



**HAL**  
open science

# Robust and efficient waveform-based velocity model building by optimal transport in the pseudotime domain: An ocean-bottom cable case study in the North Sea

Giuseppe Provenzano, Romain Brossier, Ludovic Métivier

## ► To cite this version:

Giuseppe Provenzano, Romain Brossier, Ludovic Métivier. Robust and efficient waveform-based velocity model building by optimal transport in the pseudotime domain: An ocean-bottom cable case study in the North Sea. *Geophysics*, 2024, 89 (2), pp.B83-B103. 10.1190/geo2023-0052.1 . hal-04792474

**HAL Id: hal-04792474**

**<https://hal.science/hal-04792474v1>**

Submitted on 25 Nov 2024

**HAL** is a multi-disciplinary open access archive for the deposit and dissemination of scientific research documents, whether they are published or not. The documents may come from teaching and research institutions in France or abroad, or from public or private research centers.

L'archive ouverte pluridisciplinaire **HAL**, est destinée au dépôt et à la diffusion de documents scientifiques de niveau recherche, publiés ou non, émanant des établissements d'enseignement et de recherche français ou étrangers, des laboratoires publics ou privés.

**Robust and efficient waveform-based  
velocity-model-building by optimal-transport in the  
pseudotime domain: an OBC case study in the North Sea**

**Giuseppe Provenzano<sup>\*</sup>, Romain Brossier<sup>\*</sup>, Ludovic Métivier<sup>†</sup>**

<sup>\*</sup>Univ. Grenoble Alpes, ISTerre, F-38058 Grenoble, France

<sup>†</sup>Univ. Grenoble Alpes, CNRS, LJK, F-38058 Grenoble, France

(November 25, 2024)

Running head: **Pseudotime GSOT  $V_p$  inversion**

# **Robust and efficient waveform-based velocity-model-building by optimal-transport in the pseudotime domain: an OBC case study in the North Sea**

(November 25, 2024)

Running head: **Pseudotime GSOT  $V_p$  inversion**

## **ABSTRACT**

Full waveform inversion (FWI) in the North Sea has demonstrated its imaging power starting from low-resolution models obtained by traveltime tomography, enriching them with geologically interpretable fine-scale details. However, building a traveltime-based kinematically accurate starting model for FWI is a time-consuming and rather subjective process requiring phase identification and selection. The two main problems faced by FWI starting from non-informative initial models are the liability to cycle-skipping and a lack of sensitivity to low-wavenumbers in the deep subsurface not sampled by turning waves. On a North Sea ocean-bottom-cable (OBC) 3D dataset, we apply a novel  $V_p$ -building methodology that addresses those issues by jointly inverting reflections and refractions (JFWI) using a robust misfit function in the vertical traveltime domain (pseudotime). While pseudotime addresses reflectivity-velocity coupling and attenuates phase-ambiguities at short offsets, a graph-space optimal transport (GSOT) objective function with dedicated data windowing averts cycle-skipping at intermediate-to-long offsets. A fast and balanced reflectivity reconstruction is obtained prior to JFWI thanks to an asymptotic-preconditioned Impedance

Waveform Inversion ( $I_p$ WI). Starting from a linearly increasing one-dimensional model, GSOT-pseudotime JFWI is effective at obtaining a meaningful P-wave velocity macro-model down to depths sampled by reflections only, without phase identification and picking. P-wave FWI starting from the JFWI-based model, injects the high-wavenumbers missing in the JFWI solution, attaining apparent improvements in both shallow and deep model reconstruction and imaging compared to the previous studies in the literature, and a satisfactory prediction of the ground-truth logs.

## INTRODUCTION

Full waveform inversion (FWI, Lailly, 1983; Tarantola, 1984, 1986) seeks a broadband reconstruction of the subsurface physical properties by iteratively minimizing the misfit between predicted and recorded waveforms, independent from phase labelling and picking. Waveform-based imaging is able to characterize targets with size down to half a propagated wavelength, hence having a higher resolution power than travelttime tomography, which is limited to the width of the first Fresnel zone (Woodward, 1992; Huang and Schuster, 2014). In the past decade, FWI has been applied to the characterization of subsurface targets across a range of scales: from regional seismology (10-100 km, e.g., Fichtner and Villaseñor, 2015; Davy et al., 2017; Górszczyk et al., 2021) to exploration for energy resources (2-10 km, e.g., Operto et al., 2015; Hicks et al., 2016), down to shallow site-characterization in marine as well as land settings (10-100 m, e.g., Provenzano et al., 2018; Irnaka et al., 2022).

Ideal illumination conditions for FWI are achieved when the imaging target is surrounded by sources and receivers (Virieux and Operto, 2009). Under these conditions, a full wavenumber reconstruction of the propagation medium can be obtained, as in recent applications to medical imaging (e.g. Guasch et al., 2020; Marty et al., 2021). In exploration seismic surveys, acquired at the surface above a subsurface target, FWI suffers from limited wavenumber sensitivity (Jannane et al., 1989), and is therefore highly dependent on the availability of very-low frequencies, ultra-wide source-receivers apertures, and ultimately on the quality of the starting model.

The ocean bottom cable (OBC) dataset considered in this study has been used over the past decade to showcase the resolution power of FWI, and its impact on the imaging of

complex subsurface targets at the exploration scale. Starting from a reflection traveltime P-wave velocity ( $V_p$ ) model produced by Aker BP (Sirgue et al., 2010), FWI enriches it with decametric-scale features, improving the imaging of the deep subsurface and the shallow multi-layered low velocity zone (LVZ, e.g., Sirgue et al., 2010). In particular, the improvement in resolution brought about by FWI compared to first-arrival traveltime tomography can be estimated to be in the order of the square root of the number of propagated wavelengths (Pratt and Shipp, 1999, their equation 1). In this dataset, with a maximum offset of about 15 km and for a frequency of 5 Hz, this corresponds to a reduction of the size of the smallest detectable object roughly by a factor of 5 compared to the starting long-wavelength model (Prioux et al., 2011).

In addition to a high-fidelity reconstruction of the P-wave velocity distribution in the subsurface, important insights in this survey area have been obtained about FWI multi-parameter cross-talk and sensitivity. Prioux et al. (2011) study the impact of anisotropy on isotropic one-parameter  $V_p$  inversion, demonstrating that anisotropic modelling with a vertical symmetry axis (VTI-anisotropy) is key to avoid biases in velocity-reconstruction and the consequent inaccurate reflectors imaging. They also show that accounting for viscosity, even simply through a uniform attenuation model (Quality factor,  $Q$ ), is necessary to represent the amplitude decay with offset and time. Gholami et al. (2013) study the optimal parametrization of anisotropic FWI, demonstrating the possibility to invert for  $V_p$  as long as an accurate trend of the Thomsen parameter  $\epsilon$  (Thomsen, 1986; Alkhalifah, 1997) is present in the starting model. Operto et al. (2015), in their frequency-domain 3D application, also invert for vertical  $V_p$  keeping the anisotropic parameters and attenu-

ation fixed. Kamath et al. (2021) jointly inverts  $V_p$  and attenuation quality factor ( $Q$ ), in the time-domain, showing imaging improvements with respect to constant attenuation one-parameter inversion, while  $V_p$  reconstruction benefits from a reduced acquisition footprint in multi-parameter frequency-domain inversion (Operto and Miniussi, 2018).

The aforementioned works have in common an accurate starting model of the volume around the target, obtained by reflection traveltimes tomography prior to waveform inversion. Such a model predicts the traveltimes of the main seismic phases within half a dominant period of the lowest usable frequency band in the data (about 3 Hz in the 2.5-5. Hz band, Operto et al., 2015), therefore making it possible to apply FWI using a least-squares ( $L^2$ ) waveform residuals objective function. If these conditions were not met, FWI would skip one or more oscillation cycles, driving the  $V_p$  update towards the local minimum of the objective function, and away from the optimal solution (Beydoun and Tarantola, 1988). In particular, long-offsets recording wavefronts that propagated for several wavelengths would be liable to cycle-skipping (Pratt et al., 2008).

Recently, Pladys et al. (2022) have applied  $V_p$  FWI on the same dataset, starting from linearly increasing one-dimensional  $V_p$  and density models, while including in the modelling weak anisotropy parameters ( $\epsilon$ ,  $\delta$ , Thomsen, 1986) from traveltimes-tomography and a uniform Quality factor ( $Q$ ). They demonstrated that, in this case,  $L^2$  norm inversion fails regardless of the data-weighting strategy used, while a graph-space optimal transport distance (GSOT, Métivier et al., 2019) allows FWI to achieve an acceptable model reconstruction in the shallow part of the domain (down to 2 km) with a data-domain layer-stripping strategy that includes progressively larger offsets and times.

However, regardless of the objective function used, the lack of constraints by diving waves in the deep subsurface makes it difficult to obtain reliable kinematic updates (Pladys et al., 2022). Despite the long-offsets acquired by the ocean-bottom cables in the area, the recorded diving waves do not propagate below 1.5/2.0 km (Prioux et al., 2011) and, therefore, deep  $V_p$  updates rely mostly on reflected energy. At depths sampled by reflections only, FWI provides a band-limited high-wavenumber imaging of the subsurface, similarly to an iterative least-squares migration in a fixed background velocity trend (Woodward, 1992), once more relying on the accuracy of the long-wavelengths in the starting model.

Reflection-based FWI (RWI) has the potential to obtain  $V_p$  updates below the depth sampled by diving waves, by exploiting the tomographic contribution of deep-reaching wavepaths in a reflective starting model (Xu et al., 2012; Brossier et al., 2015; Yao et al., 2020) built prior to  $V_p$  inversion by least-squares migration. In RWI, reflections act as virtual deep seismic sources that illuminate the target from below, thus filling the small-wavenumber sensitivity gap of FWI at depth (Mora, 1989) and approximating ideal subsurface illumination conditions. The idea of using RWI to inform accurate deep model updates in this area has been suggested in earlier works (e.g. in Prioux et al., 2011; Operto et al., 2015). Recently, Zhou et al. (2018) jointly inverted diving and reflected waveforms on a 2D line extracted from the 3D dataset, starting from the tomographic model and using a  $L^2$  objective function.

In this work, we attempt to reconstruct the broadband subsurface  $V_p$  using the 3D OBC hydrophone dataset and starting from a one-dimensional linearly increasing  $V_p$  model, ideally combining the objectives of Zhou et al. (2018) and Pladys et al. (2022). In order to do

so, we take advantage of the robust velocity-model building workflow presented in a companion paper (Provenzano et al., 2023) that combines: 1) joint diving and reflection FWI (JFWI) in a velocity-impedance ( $V_p - I_p$ ) parametrization, as in Zhou et al. (2018), to obtain deep velocity updates while constraining the shallow portions of the model; 2) a pseudotime (Plessix, 2013) reformulation of the JFWI gradient ensuring velocity-reflectivity consistency; 3) a GSOT objective function to ensure robustness against inaccurate starting models, as in Pladys et al. (2022); 4) an asymptotic preconditioner for fast and balanced reflectivity imaging (e.g., Li and Chauris, 2018).

We propose a challenging real-data exercise aiming to tackle cycle skipping and lack of deep velocity sensitivity starting from an almost blind guess of  $V_p$  and density. After briefly recalling the key aspects of the methodology described in Provenzano et al. (2023), we show that, using minimal pre-processing, the JFWI-based strategy is effective at obtaining a meaningful low-frequency model consistent with the one provided by Aker BP, but in a purely waveform-based fashion, without phase identification and picking. The JFWI provides an improved prediction of the P-wave velocity trends contained in three sonic logs available in the acquisition area, in particular close to the exploration target. Mono-parameter  $V_p$ -FWI, starting from the JFWI-based model, complements the JFWI solution with additional high-wavenumbers, attaining improvements in both shallow and deep model broadband imaging compared to conventional FWI.

## OVERVIEW OF DATASETS AND MODELS

The survey area is located in the Norwegian North Sea, with an approximately constant water depth of 70 m. An anticline structure between 2.5 and 3.5 km is overlaid by weakly tectonized, almost plane-parallel multi-layered low-velocity zone between 1.5 and 2.5 km (hereafter referred to as LVZ). Shallow ( $< 300$  m depth) riverbed channel structures, as well as near-vertical low-velocity zones ( $< 1$  km depth) have been imaged by recent FWI applications (e.g., Operto et al., 2015; Kamath et al., 2021).

The four-component (4C) ocean-bottom-cable (OBC) dataset, acquired in 2011, covers an area of  $145 \text{ km}^2$ , and consists of 50824 shots fired at 5 m below the sea surface with 50 m spacing. The acquisition system is made up of 2049 receivers with 50 m in-line spacing and 300 m cable-spacing (Figure 1), for a maximum absolute offset of about 15 km. In this study, we work on the hydrophone component of the 4C system, with a useful bandwidth starting from 2.5 Hz. Three sonic logs, one proximal to the target area, the remaining two at the margin of the survey, are going to be used to quality check our estimated P-wave velocity ( $V_p$ ).

The feasibility of acoustic FWI on the hydrophone-component of this OBC dataset has been shown by Brossier et al. (2009), by virtue of the weak imprint of P-S converted waves on the pressure component in a subsurface containing relatively mild S-wave contrasts (Operto et al., 2015). In this study, we invert the hydrophone data for vertical P-wave velocity ( $V_p$ ) in a visco-acoustic anisotropic subsurface, while keeping the other parameters fixed (Pladys et al., 2022).

The starting acoustic properties are described by 1D linearly increasing velocity ( $V_p$ , Figure 4) and density ( $\rho$ ) (Pladys et al., 2022), therefore lacking key low-wavenumber information and exposing conventional FWI to cycle-skipping at offsets as low as 3 km. Although an analysis of the first-arrivals kinematics would make it possible to build a better initial model, this work aims at testing the methodology proposed in Provenzano et al. (2023) in a particularly challenging context, starting from an almost-blind guess (as in Pladys et al. (2022)).

In the attempt to attain an accurate  $V_p$  reconstruction from such a poor initial model, accounting for anisotropy is however key to avoid over-/under-estimating vertical  $V_p$  in the shallow subsurface. In particular, Prieux et al. (2011) and Gholami et al. (2013) show that it is possible to invert for vertical  $V_p$  in a  $[V_p, \epsilon, \delta]$  parametrization as long as the long-wavelength trend of  $\epsilon$  is correct in the starting model, while  $\delta$  has little impact (Thomsen, 1986). Therefore, we include in the starting model the tomographic smooth weak anisotropy ( $\epsilon, \delta$ ) provided by Aker BP. Their ellipticity model ( $\eta = \frac{\epsilon - \delta}{1 + 2\delta}$ , Alkhalifah, 1997), presented in Figure 3, accounts for a relative change between horizontal and vertical  $V_p$  reaching 15% at the reservoir level. Finally, a visco-acoustic modelling with homogeneous Quality factor ( $Q$ ) equal to 200 is employed to appropriately account for the wavefield's amplitude decay with time and offset (Operto and Miniussi, 2018; Kamath et al., 2021).

Despite the availability of large source-receiver offsets in the OBC dataset, subsurface depths greater than 1.5 km are mostly sampled by reflections (Prieux et al., 2011; Operto et al., 2015). Therefore, FWI provides a band-limited update of  $V_p$  both at the reservoir level and the multi-layered LVZ, due to the narrow-angle available wavepaths (Woodward,

1992). In order to overcome this limitation, we will take advantage of the tomographic contribution of reflections in a reconstructed reflective model, jointly with diving waves (Zhou et al., 2015). In this context, the methodology outlined in the following section addresses three fundamental issues of reflection-driven velocity model building starting from a poor initial model (Provenzano et al., 2023): 1) ensuring consistency between fixed reflectivity and evolving model kinematics in  $V_p$  inversion; 2) minimizing the risk of cycle skipping; 3) minimizing the cost of building the initial reflective model.

## OUTLINE OF THE METHOD

### Efficient Joint FWI in pseudotime

JFWI (Zhou et al., 2015) simultaneously inverts reflected and refracted waves, in order to enrich the sensitivity kernel of diving waves with deep-reaching transmission-regime reflection wavepaths (Huang and Schuster, 2014). Scale separation between the desired tomographic updates and the high-wavenumber reflective components of the model is achieved by suppressing the migration isochrones (Zhou et al., 2015), in combination with a velocity-impedance ( $V_p$ - $I_p$ ) parametrization (Operto et al., 2013). The JFWI objective function thus results from the weighted contributions of early arrivals ( $e$ ) and reflections ( $r$ ):

$$f(V_p) = G(W^e d_{cal}^e, W^e d_{obs}^e) + G(W^r d_{cal}^r, W^r d_{obs}^r). \quad (1)$$

In the latter,  $G$  is a generic misfit function,  $W^e$  and  $W^r$  are data weighting matrices selecting and scaling early arrivals and reflections (Figure 2c,d),  $d_{obs}$  and  $d_{cal}$  indicate respectively the observed and synthetic data sampled at the receivers position. In particular,  $d_{cal}^e$  is the background ( $u_0$ ) synthetic wavefield computed in the smooth starting model, while  $d_{cal}^r$  is the reflected wavefield ( $\delta u$ ) computed in the reflective starting model, whose discontinuities are contained in  $I_p$ .

Using  $u$  to indicate the forward fields and  $\lambda$  for the adjoint fields, the JFWI gradient with respect to  $V_p$  can be written as:

$$\nabla f(V_p) = u_0 \star \lambda_0^e + u_0 \star \delta \lambda^r + \delta u \star \lambda_0^r + \delta u \star \delta \lambda^r, \quad (2)$$

where the  $\star$  operator encompasses the time-convolution and the partial derivative with respect to  $V_p$ . In the right hand side, we can recognize the following contributions to the JFWI gradient: 1) an early-arrival kernel obtained by correlating the incident field  $u_0$  and the incident adjoint  $\lambda_0^e$  generated by the diving wave residuals; 2) a source-to-reflector RWI kernel resulting from the correlation of the incident wavefield  $u_0$  and the scattered reflection adjoint wavefield  $\delta \lambda^r$ ; 3) a receiver-to-reflector RWI kernel produced by correlation of the scattered primary wavefield  $\delta u$  and the incident reflection adjoint field  $\lambda_0^r$ ; 4) the last terms represents higher order scattering contributions.

Convergence of JFWI is however made difficult by the dependency of  $I_p$  on  $V_p$ , namely between the reconstructed reflectors geometry and model kinematics. We propose a reformulation of JFWI in the vertical traveltime (pseudotime,  $\tau$ ) domain (Rickett and Childs, 2011), following Plessix (2013) and Brossier et al. (2015). This makes it possible to en-

force the zero-offset time invariance by keeping the reflective  $I_p$  model fixed in pseudotime rather than in depth, hence reducing phase ambiguities at short-offsets. At each iteration, modeling and computation of the JFWI gradient are performed in depth (as in equation 2) and mapped to pseudotime by using the derivative chain rule (Plessix, 2013); both the updated  $V_p$  and the invariant  $I_p$  in time are then re-mapped to depth using a linear interpolation scheme in the modeling grid. Thereby, reflectors in  $I_p$  are repositioned at each iteration, reducing the need for iterative least-squares migrations (Provenzano et al., 2023) and therefore containing the computing cost. Two model-dependent pseudotime axis parameters are defined, namely the maximum expected travelttime and the time step, preferably so that the sea-floor reflection is an integer multiple of the latter. The one-dimensional time-to-depth transform is however sub-optimal in models with steep structural dips and strong lateral variations, where the need for reverse-time reflection imaging cannot be altogether eliminated.

In order to speed-up the reconstruction of the reflective model by impedance waveform inversion ( $I_p$ WI), a dedicated asymptotic-preconditioned  $I_p$  gradient is employed (Provenzano et al., 2023). Originally based on the inverse scattering theory for the asymptotic linearized wavefield (Beylkin, 1985), this approach relies only on wavefield quantities (Qin et al., 2015; Li and Chauris, 2018; Farshad and Chauris, 2021) to scale and weight the  $I_p$ WI gradient in the framework of an iterative least-squares inversion. Unlike in previous approaches (Li et al., 2019), the proposed asymptotic  $I_p$ WI implements a true frequency-domain deconvolution imaging condition (Schleicher et al., 2008) within the time-domain waveform inversion framework, thanks to the decimation and storage on the fly of the for-

ward and adjoint wavefields in the discrete-Fourier-domain (DFT, Yong et al., 2022). This makes it possible to obtain sharp and balanced impedance models at a fraction of the time, and within reasonable memory requirements (Provenzano et al., 2023).

## Graph space optimal transport against cycle skipping

While the pseudotime approach avoids phase ambiguity at near-zero offsets, a graph-space OT (Métivier et al., 2019; Métivier and Brossier, 2021) objective function is used in order to reduce the liability to cycle-skipping at intermediate-to-long offsets. In GSOT, seismic traces are transformed from oscillatory signals into two-dimensional discrete distributions of  $K$  unit-weight points in the time-amplitude graph-space, where  $K$  is the number of samples after Nyquist resampling. An assignment problem between the observed  $(t(j), d_{obs}(j))$  and predicted  $(t(i), d_{cal}(i))$  trace is solved for the optimal permutation plan  $\sigma^*$ , which connects each sample of the initial distribution to a sample in the target one. In the graph-space, the 2-Wasserstein distance between the two distributions is thus defined as:

$$h_{W^2} = \sum_{i=1}^K \frac{A^2}{\Delta_t^2} |t_i - t_{\sigma^*(i)}|^2 + |d_i^{cal} - d_{\sigma^*(i)}^{obs}|^2, \quad (3)$$

where the time axis is scaled by the ratio between the maximum expected time shift  $\Delta t$  and the maximum amplitude  $A$  difference between observed and predicted data. Among all possible  $i - j$  permutations,  $\sigma^*$  minimizes the work needed to transport the predicted data points distribution into the observed one (Kantorovich, 1942). Convexity with respect to time-shifts is given by the monotonic dependency of the transport work on the terms  $|t_i - t_j|^2$ .

In JFWI, the reflection and diving wave optimal transport distances are computed independently, to honor the differences in amplitude range between the two propagation regimes. The objective function in equation 1 can be re-written using equation 3 as:

$$f(V_p) = \sum_{shot} [W^e h_{W^2}^r(\sigma^{div*}) + W^r h_{W^2}^e(\sigma^{refl*})]. \quad (4)$$

Each propagation regime has its own optimal transport plan in a specific graph space scaled by  $A_{div}$  and  $A_{refl}$  respectively, with the possibility of defining different maxima expected time-shifts  $\Delta t$  if, for example, a larger one should be used for diving waves than for reflections (Provenzano et al., 2023).

In equation 3, large  $\Delta t$  values emphasize the convexity with respect to shifted patterns and therefore help to mitigate cycle skipping, whereas, as  $\Delta t$  decreases, each  $\sigma^*$  tends to a local sample-by-sample mapping ( $\sigma^*(i) = i$ ), and  $h_{W^2}$  approximates the behavior of the  $L^2$  distance.  $L^2$  can be therefore viewed as a special case of GSOT distance for  $\Delta t=0$ , in which the adjoint sources are simply the reflection and diving wave residuals. Such flexibility can be exploited to fine-tune the behaviour of the objective function during inversion: large  $\Delta t$  values may enhance robustness at early iterations, when kinematic mismatches are large, and can then be reduced as wavefield prediction improves and it becomes desirable to approximate the resolution of  $L^2$ -norm

# JFWI-BASED $V_P$ INVERSION

## Modelling

In order to predict the hydrophone component of the OBC dataset, modelling is performed in the time-domain using a first-order formulation of the wave equation (Yang et al., 2016a), within a visco-acoustic VTI anisotropic approximation. In the latter, attenuation is implemented using a generalized standard linear solid (SLS) mechanical model (Yang et al., 2016a), with a combination of 3 relaxation mechanism at frequencies equal to 1, 6.32 and 40 Hz, to approximate a constant quality factor (Q) within the frequency band of interest (Blanch et al., 1995; Yang et al., 2018), as in Kamath et al. (2021).

The finite-difference discretization is performed using a fourth-order in space and second-order in time staggered grid. The nearly flat topography makes the finite-difference method suitable in this setting. The models are discretized in space with  $\Delta x = 70$  m for the 2.5-5 Hz band, to ensure at least 5 grid points per wavelength for the smallest velocity, and  $\Delta t$  is chosen accordingly to enforce the CFL (Courant-Friedrichs-Lewy) stability conditions for explicit schemes. Windowed cardinal sine interpolation is used to simulate source and receivers positions falling in between grid points (Hicks, 2002).

A flat free surface condition is applied at the top of the model to represent the water/air interface and include ghosts and multiples in the predicted data, since they are not removed from the field data in pre-processing. Sponge layers (Cerjan et al., 1985) are applied in the other directions to simulate an infinite-extension medium and thus attenuate off-boundary reflections. This choice aims at avoiding instabilities of perfectly-matching-layer boundary

conditions (PML, Bérenger, 1994) that may arise in acoustic anisotropic media (e.g. Beccache et al., 2003, 2010). Finally, in order to have an efficient and stable computation of the gradient in a visco-acoustic medium, we rely on a checkpoint-assisted reverse forward simulation approach (CARFS, Yang et al., 2016b), which ensures stability and reduces the re-computation ratio compared to purely checkpointing-based approaches.

## **Data pre-processing and windowing**

Since the number of sources in the survey is around 25 times larger than the number of receivers, reciprocity between sources and receivers is applied, in order to reduce the computing cost by taking advantage of the shot-based parallelization of the inversion code. Gatherers with anomalous root-mean-square (RMS) energy are identified and eliminated, reducing the number of sources, after reciprocity, from 2049 to 2044. Data pre-processing is limited to minimum-phase bandpass frequency filtering, followed by muting of Scholte waves (Kamath et al., 2021; Pladys et al., 2022), since they cannot be modelled in our visco-acoustic approximation. The inversion is performed on the 2.5-5.Hz frequency band, decimated to a 8 ms sampling rate.

In such narrow frequency bands, separation between turning waves and reflected arrivals can be cumbersome; on top of that, the presence of multi-refracted guided waves in the shallow subsurface (shingling waves, Robertson et al., 1996) contaminates the diving waves with steep-sloping slow arrivals. Therefore, in order to design an appropriate windowing, data computation in a reflection free model is performed to identify an acceptable time-offset separation between the two propagation regimes. A taper zone of 0.2 seconds

is applied, to avoid contaminating the reflection window with the aforementioned near-surface effects, and to allow for changes in traveltimes during inversion. For simplicity, the same windowing function is used for every shot.

A shot-averaged source wavelet is estimated (Figure 2a) at the beginning of each inversion stage, using the frequency domain method proposed by Pratt (1999). The latter is a linear inverse problem for a set of wavelet coefficients, which assumes the predicted Green's function to be equal to the observed one. In order to minimize the impact of an incorrect subsurface model on the wavelet estimation, only the near offset, short time data are used for this task, as in Kamath et al. (2021) and Pladys et al. (2022). In Figure 2, the different data portions used for source estimation (Figure 2a), impedance inversion ( $I_p$ WI, Figure 2b), and velocity reconstruction (JFWI) are presented (Figure 2c for reflections, Figure 2d for diving waves.)

[Figure 1 about here.]

[Figure 2 about here.]

## **Inversion**

[Table 1 about here.]

Despite the convexity of GSOT with respect to time-shifts, offset-windowing in  $V_p$  inversion is beneficial when starting from such a crude model (Figure 4). This helps avert

cycle-skipping induced local-minima entrapment, while ensuring a reasonable convergence speed (Górszczyk et al., 2021; Pladys et al., 2022).

The 1D starting model predicts heavily cycle-skipped diving waves even at offsets shorter than 3 km (Figure 13a) as a consequence of the inaccurate shallow subsurface velocities. Therefore, it has been found beneficial to start the inversion workflow with a conventional diving wave  $V_p$ -FWI at offsets shorter than 4.8 km, taken to be equivalent to the first step of Pladys et al. (2022), and only later start the reflection-based velocity model building with JFWI. The 4.8 km offset threshold has been found empirically to correspond to a synthetic-to-observed traveltimes mismatch GSOT can handle, without overly increasing  $\Delta t$  (equation 3) thus jeopardizing convergence in the presence of noise (Métivier and Brossier, 2021)

In the preliminary FWI stage, random 128-shot subsamples are drawn and inverted for 3 limited-memory BFGS (Nocedal, 1980) iterations with illumination-compensation preconditioning (Kamath et al., 2021), for a total of 101 iterations so that every source is drawn at least twice. The resulting model is smoothed using a 3D Gaussian filter with lengths equal to the wavelength at 1.5 km/s, to obtain a suitable kinematic model rid of high-wavenumbers (Figure 5) that would otherwise pollute  $V_p$ . This is followed by  $I_p$ WI to build the initial reflective model that will inform JFWI kernel with deep-reaching wavepath and, finally, by FWI.

Table 1 summarizes the stages of the adopted inversion strategy and the values of the most relevant tuning parameters. Within the multi-stage JFWI+FWI workflow, the philosophy is to progressively include larger offsets, increase the deeper contributions to the

gradient by preconditioning and reduce the GSOT- $\Delta t$  (equation 3) to approximate an  $L^2$  behaviour as model kinematics improves.

It is worth pointing out two major differences between the preliminary stage and the JFWI-based velocity model building. Firstly, the size of the random source subset is changed to 256, purely because of the different node-architecture of the cluster used compared to the short-offset diving wave step by Pladys et al. (2022). More importantly, the optimization method is changed from l-BFGS to a preconditioned steepest-descent. As pointed out in Zhou et al. (2018), steepest descent ensures slower but more robust updates in reflection-based inversion in the presence of noise (e.g., Dagnino et al., 2016), both random and coherent (e.g., ghosts and multiples), a situation in which l-BFGS may collect inaccurate information about the curvature of the objective function from the previously computed gradients (Métivier and Brossier, 2016).

### *$I_p$ reconstruction*

Velocity model building starts with  $I_p$ WI of the short spread reflections, with source-receiver offsets smaller than 3 km (Figure 2b), taking advantage of the proposed pseudo-asymptotic wavefield-based preconditioner. Two iterations are performed for each 256-shot random batch, for a total of 16 iterations, such that each available shot gather is sampled at least once. Within the 2.5-5 Hz band, 12 frequencies are stored to compute the preconditioned gradient, which is 1/4 of the Nyquist number of samples at 5 Hz and yet sufficient to avoid wrap around effects in the computed  $I_p$  update (Yong et al., 2022). A larger number of frequencies did not improve substantially the final model quality, whereas a number

of frequencies lower than 10 would create artefacts in the  $I_p$  gradient as wrap-arounds of the deep structures into the shallow ones. This number is largely data-dependent, and requires an educated user choice; however, it is qualitatively proportional to the wavefield complexity (Yong et al., 2022).

In Figure 6 the advantages of the proposed preconditioner are apparent in a higher convergence rate compared to a wavefield-based illumination compensation (Kamath et al., 2021), by virtue of the deconvolution imaging condition and the inherent wavenumber filtering. This corresponds to a sharper and more balanced final reflective model (Figure 7), while the conventional preconditioning would require a larger number of iterations to converge to a comparable solution. The proposed preconditioner is thus key in obtaining, in a limited number of iterations, a suitable starting reflective model for JFWI (Zhou et al., 2018).

### $V_p$ JFWI

After  $I_p$ WI, JFWI is first run on offsets shorter than 7 km for 24 steepest descent (ST) iterations, 3 for each 256-shot random batch. The weight of the diving waves term is 2-times as large as the one of reflections, in order to privilege shallow kinematic updates in the earlier iterations. Even so, the added value of reflections compared to conventional FWI at depths larger than 1.5 km is apparent when comparing this stage's JFWI with the initial early-arrivals FWI model (Figure 8).

The offset window is then relaxed to include offsets up to 9 km and one more JFWI run is performed with the same number of ST iterations; diving and reflected waves are now

given the same weight in the objective function, in order to respect the natural scaling of the two propagation regimes in the data. A final JFWI step is then performed on the whole offset range (Figure 9).

Combined with offset-selection, a depth-dependent gain is applied to the JFWI gradient as a preconditioner after conversion to pseudotime, progressively increasing the depth power from 1 to 2 as the inversion proceeds to the following step, in order to privilege deep velocity updates after meaningful shallow updates have been obtained.

The GSOT maximum expected time-shift ( $\Delta t$ ) is set to 0.35 s at the first two JFWI stages, and then reduced to 0.25 s in the diving window and to 0.125 s in the reflection one. The choice of a variable  $\Delta t$  across the inversion stages serves the purpose of enhancing convexity with respect to time-shifts at the beginning, and later approximate the behaviour of a  $L^2$ -norm inversion as the model kinematics improves; the use of a shorter  $\Delta t$  in the reflection window is, on the other hand, justified by the lower maximum expected time shift between predicted and observed reflection moveout compared to that of diving wave traveltimes.

In this pseudotime formulation of JFWI,  $I_p$  is updated in depth simultaneously with  $V_p$ , without requiring repeated runs of  $I_p$ WI to ensure consistency between kinematics and reflectivity at short offsets. However, intermediate fast (8 iterations, 1 per source random batch)  $I_p$ WI steps are interleaved in between offset-range JFWI runs starting from the pseudotime-updated impedance, in order to adjust the amplitude of the impedance contrasts and make up for possible losses of structure during resampling from depth to pseudotime.

The intermediate and final JFWI models are shown in Figure 8 and 9. Note that the JFWI- $V_p$  contains structures consistent with the ones in the tomographic model (Figure 10), though entirely based on waveform inversion and without requiring travetime picking. The inversion will then proceed with a conventional FWI step starting from the final JFWI  $V_p$  model, first with offsets shorter than 9 km, then including all offsets.

[Figure 3 about here.]

[Figure 4 about here.]

[Figure 5 about here.]

[Figure 6 about here.]

[Figure 7 about here.]

[Figure 8 about here.]

[Figure 9 about here.]

[Figure 10 about here.]

[Figure 11 about here.]

[Figure 12 about here.]

## $V_p$ FWI

After three JFWI runs with widening offset windows,  $V_p$  FWI starts in the same frequency band to inject higher spatial frequencies into the velocity macromodel, thus broadening the bandwidth of the reconstructed subsurface model. For this aim, the parametrization is changed from  $[V_p, I_p]$  to  $[V_p, \text{density } (\rho)]$  (Operto et al., 2013), where  $\rho$  is re-set to its initial value, since density after JFWI in the  $[V_p, I_p]$  parametrization has no physical meaning. FWI is performed for 48 l-BFGS iterations (Nocedal, 1980) with wavefield preconditioning (Kamath et al., 2021) in two steps, the first with offsets shorter than 9 km, the second including all offsets. Partitioned into 3 iterations per 256-shot batch, this corresponds to 2 epochs of full data sampling per stage. GSOT distance is used at this stage, with  $\Delta t$  equal to 0.25 in the 9 km window and reduced then to 0.2 in the full-offset one.

The results of FWI following JFWI are shown in Figure 11. We compare them in Figure 12 with the model obtained by conventional FWI starting from the 1D model by Pladys et al. (2022) with a 6-step data-domain layer stripping strategy that progressively included larger offsets and time. The contribution of JFWI to FWI (Figure 11) is apparent at depths larger than 1.5 km, where a wider LVZ is reconstructed, while a deep high-velocity anticline is obtained below the LVZ consistent with the tomographic model (Figure 10). Conventional FWI (Figure 12), on the contrary, fails to update the model away from the 1D starting model at those depths not sampled by turning waves. This is apparent also on the vertical profiles extracted at the LVZ location and shown in Figures 9, 10, 11 and 12.

We will now ascertain whether the updated JFWI+FWI model is necessary to better

explain the data and the independent ground-truth information available in the target area.

## Quality checks

### *Data domain*

The first quality check is performed on the waveform fit of two control 2D lines extracted from two common receiver gathers, one proximal to the LVZ (cable A), the other one away from it (cable B). Modelling is performed using the same source wavelet (the one estimated in the first JFWI stage) in order to make the comparison consistent. In Figures 13 and 14, an alternating view of field and synthetic traces is presented to showcase the waveform fit for: a) the starting model, b) the short-offset EWI+ $I_p$ WI, and c) JFWI. Wiggle overlays at randomly selected traces at a range of offsets are also plotted to better appreciate phase and amplitude changes. It is worth pointing out the important traveltime difference between predicted and observed data at offsets as short as 2.5 km in a), that would expose  $L^2$  inversion to cycle-skipping. After the very-short offset diving waves are fit by early-wave GSOT-EWI (b), GSOT-JFWI, along with  $I_p$ WI and the pseudotime formulation, improves the waveform fit for both diving and reflected waves, both in phase and amplitude (c).

In Figures 15 and 16, a comparison is presented between the data prediction of JFWI+FWI (panels a) and the 6-step layer-stripping conventional GSOT-FWI (panels b) by Pladys et al. (2022) starting from the same initial model. Marginal improvements in data prediction are observed for JFWI+FWI compared to conventional FWI, mostly for larger offset reflections, namely at times larger than 5 seconds and offsets between 4 and 7 km. In particular,

reflection amplitude prediction is improved in the JFWI+FWI model, despite the fact that both cases use the same density model. While the long-offset diving waves at offsets larger than 9 km seem to be slightly better predicted by conventional FWI in cable B (Figure 16b), the improvement in long offset fit in cable A (proximal to the low-velocity cloud) is striking at long offsets, as it appears in the wiggle plot at 9.5 km (Figure 15a).

In order to provide an alternative more quantitative evaluation of data prediction over the whole target, we compute the zero-lag correlation between the predicted and observed data for the same two control common receiver gathers, again using the same source wavelet. In Figure 17 the improvement in waveform coherency between the initial and final JFWI+FWI model is striking, while the comparison with the results of conventional FWI is non-conclusive (a relative increment of -1.5% for receiver A and +1% for receiver B).

The same comparison is then performed selecting the reflection time-offset window (Figure 18). In this case, the improvement in waveform coherency of the JFWI+FWI data is more apparent and results in a higher average cross-correlation value: +7% for receiver A and +3% for receiver B. This posterior data prediction analysis confirms the role of reflections in velocity model building; on the other hand, the fact that the average cross-correlation values on the whole dataset are similar (within a 1.5% tolerance) suggests that conventional FWI ensures marginally better waveform coherency in the diving window, as expected by a velocity model updated mostly by refractions.

In the exact subsurface model, the estimated source wavelet using the frequency domain method by Pratt (1999) is independent of the location within the survey, since the pre-

dicted and observed Green's functions should be identical in the frequency band and offset range of interest. Otherwise, the estimated wavelet coefficients collect the space-dependent Green's functions' inaccuracies as they result from an inaccurate subsurface model. Such an attribute can thus be exploited to assess the quality of a model (Operto and Miniussi, 2018). Here, the stationarity of the wavelet estimation across a random selection of common receiver gathers is evaluated in the initial, FWI and JFWI+FWI final  $V_p$  models on the whole time-offset range. Figure 19 shows an apparent improvement in model quality between the initial and both the JFWI+FWI and FWI inverted models. The sum of the least-squares residuals between the wavelets and their average, i.e. their variance, confirms that the JFWI+FWI model ensures a better wavelet stationarity than the conventional FWI one, which is consistent with a better approximation of the true model. Furthermore, the onset of the average estimated wavelet in the JFWI+FWI model is closer to the reference wavelet used for inversion (red vs white wavelet envelopes in Figure 19)

### *Ground-truthing*

In Figure 20, we compare the inverted velocities with the ground-truth of the three available sonic logs, low-pass filtered within half a period for the maximum frequency used in the inversion (5 Hz), and against the reference kinematic model by Aker BP. As pointed out in Pladys et al. (2022), GSOT makes it possible for FWI to attain sensible improvements despite the very simple starting model down to around 1.5 km depth. Below, the contribution of reflections becomes apparent, in particular for Log-1, proximal to the LVZ (Figure 1), where JFWI captures a velocity reduction consistent with the sonic velocities, while FWI

only adds high-wavenumbers to the initial trend. For Log-2, predictions are not entirely satisfactory, which may result from the poor illumination at the margin of the acquisition layout (Figure 1). Here FWI seems to outperform JFWI, since it remains locked to the starting model at depth, where the latter happens to be closer to the sonic velocities. It is worth pointing out how the reference tomographic model underestimates Log-2 below 2 km depth similarly to JFWI. As for Log-3, JFWI produces velocity updates consistent with the tomographic model, and outperforms FWI at depths larger than 1.5 km.

In Figure 21, the correlation coefficients between the low-pass filtered logs and the inverted  $V_p$  are plotted. In Log-2, although the FWI prediction is closer in absolute value to the ground-truth, JFWI produces a better-correlated profile. The results for Logs 1 and 3, instead, are unambiguous both in absolute distance and correlation value.

The tomographic model seems to outperform both FWI and JFWI in the top 800 meters (Logs 2 and 3 in Figures 21), probably due to the impact of the short-period sea-surface multiples and inaccurate densities in the shallow subsurface, making it difficult for the waveform methods to retrieve the velocity trend, approximating it instead with oscillating patterns.

### *Image domain*

Common image gathers (CIGs) are built by two-dimensional reverse-time-migration (RTM) on a section of the model extracted along receiver-cable A, going over the LVZ cloud. Band-pass filter between 2.5 and 10 Hz is applied to the selected 160 common-receiver gathers, along with 3D to 2D conversion for amplitude ( $\sqrt{t}$  factor as in, e.g., Hicks and

Pratt (2001)) and FK-filter to remove Scholte waves in the reflection window. The wavelet is re-estimated to absorb 3D-2D phase effects, and 26 offset classes are migrated between 0 and 6 km. In Figure 22, the 2D RTM CIGs for the starting 1D model (a), conventional FWI (b), JFWI+FWI (c) and reference tomography (d) are compared at an interval of 750 metres along the extracted line, in a west-to-east range between 5.5 and 12.5 km (Figure 1). Note that the FWI model (b) flattens the CIGs at shallow depths, correcting for the consistent under-estimation in the starting one (a). However, the lack of deeper velocity updates in FWI is such that reflectors are bent downwards (velocity over-estimation) compared to the relatively flat reconstruction in the starting model (a). On the contrary, JFWI (c) seems to correct the reflection image move-out at a broader range of depths, corroborating the results from data-domain and ground-truth QC. However, some velocity under-/over-estimations in the JFWI model are present, in particular in the rightmost part, and the tomography model (d) remains a benchmark for this case study, with excellent overall CIGs flattening. Nevertheless, in some instances (see white arrows in Figure 22), JFWI seems to ensure better flattening than both FWI and the reference tomographic model.

Stacking CIGs in Figure 22 produces the migration images in Figure 23. RTM in the JFWI+FWI model (c) yields a structural reconstruction closer to the reference tomo (d), with improved deeper imaging (e.g. at 2.5 km) compared to conventional FWI (b), which only marginally improves compared to the 1D model (a). Consistent with the observations on the CIGs, imaging quality seems to be the most reliable in the reference tomographic model.

[Figure 13 about here.]

[Figure 14 about here.]

[Figure 15 about here.]

[Figure 16 about here.]

[Figure 17 about here.]

[Figure 18 about here.]

[Figure 19 about here.]

[Figure 20 about here.]

[Figure 21 about here.]

[Figure 22 about here.]

[Figure 23 about here.]

## **DISCUSSION**

Starting from a crude one-dimensional model, graph-space optimal transport (GSOT) can mitigate significantly cycle-skipping with respect to  $L^2$ -norm (Pladys et al., 2022), but the missing low-wavenumbers cannot be fully retrieved at depth by conventional FWI regardless of the objective function employed. The results presented here show that velocity is

constrained by diving waves down to the top of the LVZ, while the tomographic contribution of reflections has to be explicitly accounted for to image accurately any deeper (Prioux et al., 2011).

An obvious advantage of Joint FWI over RWI is that it retains the constraints of diving waves down to 1.5 km depth, while deeper reflection-driven updates benefit from a better constrained shallow model. In addition, in areas of the subsurface sampled by both reflections and refractions, the latter stabilize the inversion results where surface-related multiples and elastic effects are present (Provenzano et al., 2023). This makes it possible to invert the data with minimal pre-processing, i.e. no multiple suppression or de-ghosting, and within the visco-acoustic approximation, despite expected elastic effects (e.g. AVO) in the LVZ reflections.

The results of FWI following JFWI are comparable with the ones obtained in Pladys et al. (2022) down to 1.5 km, but are richer in low-wavenumbers below this depth thanks to the tomographic contribution of reflections. The low wavenumbers injected by JFWI into FWI are closer to the ones contained in the reference traveltime-tomography model, though driven entirely by waveform inversion. This is apparent in the delineation of the anticline structure below the LVZ, which is absent in the FWI-only results, as well as in a superior fit with the sonic log velocities. The ground-truth is predicted with high-fidelity within the expected vertical resolution (Figure 20) especially close to the LVZ, showing independence from the low-frequencies contained in the 1D linearly-increasing initial model.

The quality of the data fit at the two control shot lines vouch for the accuracy of the obtained subsurface model, as shown in the waveform comparison (Figures 13 and 14),

as well as in the zero-lag correlation image between observed and predicted seismograms (Figures 17 and 18). Though for the whole time-offset range the quality of JFWI+FWI and FWI-only predictions is hardly distinguishable, long-offset fit for JFWI+FWI seems to be superior, in particular for the gather proximal to the LVZ (cable A). Furthermore, the cross-correlation performed on the reflection window shows better phase prediction for the JFWI+FWI model. The cross-correlation results for the two common receiver gathers are worth commenting on. Receiver A is closer to the LVZ area and has thus stronger reflections, implicitly posing a higher weight to the reflection term of the JFWI objective function, which might explain the difference in cross-correlation value between the diving and reflection window. Ideally, a gather-dependent objective function weighting would thus be required to account for space-dependent reflection and diving amplitude scaling.

The migration-based quality check (Figure 22 and 23) confirms a better quality of the JFWI+FWI model with respect to the starting 1D as well as to conventional FWI. However, the imaging quality obtained in the estimated  $V_p$ s seem to be lower than the one ensured by the reference tomographic model (Figure 23). This could be attributed to a number of factors that may hinder the effectiveness of our waveform-based method over a kinematic one in retrieving a purely tomographic model update from reflections, e.g.: the imperfect reflection-diving separation may pollute with unwanted high-wavenumber components the JFWI gradient (equation 1 and Figure 2); high-wavenumber features may be introduced also by the higher-order scattering term in equation 2; the impact of converted P-S-P waves may challenge the acoustic approximation used. In addition, both waveform methods seem to suffer from an imperfect reconstruction of the shallow velocities (see for example log-3

in Figure 20), which JFWI can only partially make up for by including reflections. This may reflect the impact of inaccurate densities and/or shallow-water multiples, both on wavelet estimation and model parameter inversion. Better constrained shallow densities (e.g. aided by density-logs) and additional pre-processing (e.g. surface-related multiple attenuation) may in principle reduce the shallow-model inaccuracies observed in this case study, and thus their impact on the quality and repeatability of the solution.

Solution uncertainties may be estimated quantitatively, in order to shed light on the reliability of some of the unconfirmed patterns in the reconstructed model. Data-assimilation approaches, such as Ensemble Kalman filters (Thurin et al., 2019), are a potential candidate to access a low-rank approximation of the posterior covariance matrix. While Monte Carlo Markov Chain analysis (MCMs, Sambridge and Mosegaard, 2002) would be computationally intractable, Hamiltonian MCMC (H-MCMC) approaches may be a viable alternative to explore the solution null-space, thanks to their hybrid local-global nature (e.g., Keating and Innanen, 2021), similarly to variational inference approaches (Zhang and Curtis, 2020) in a re-parametrized low-dimensional space (e.g., Ray et al., 2016).

In an anisotropic subsurface, while the turning waves in the early-arrival term of JFWI are more sensitive to the shallow horizontal  $V_p$ , the kinematics of the near-vertically propagating reflections would be controlled by vertical  $V_p$ ; therefore, when inverting for vertical  $V_p$  only, it is crucial in JFWI to rely on anisotropic modelling within an accurate  $\epsilon$  macro-model. Here we use  $\epsilon, \delta$  weak anisotropy model derived from the travelttime-based tomography by Aker BP, though future work will explore the possibility to invert for anisotropic velocity by JFWI with an appropriate model parametrization (Gholami et al., 2013).

The waveform-based asymptotic preconditioner, used in  $I_p$ WI, is key in this case study to obtain a fast and balanced reflective image (Figures 6 and 7), thanks to the deconvolution imaging condition implemented in the decimated DFT domain (Yong et al., 2022; Provenzano et al., 2023). As shown by Zhou et al. (2018), the accuracy of the starting reflective model is crucial for JFWI to converge to the true model kinematics. In this paper, we build the impedance model once at the beginning of the workflow in the starting velocity model, and then let it evolve in the pseudotime domain during JFWI, interleaving fast  $I_p$ WI (1 iteration per random sources batch) refinements after each offset group, to compensate for potential inaccuracies arising from anisotropy and resampling from depth to pseudotime domain and back. Such intermediate fast  $I_p$ WI steps are beneficial to make up for losses of continuity of the reflectors that can be attributed to the effects of VTI anisotropy in a depth-to-time stretching that only accounts for vertical velocity.

The pseudotime approach (Plessix, 2013) is a computationally- and memory-cheap alternative to migration-based-traveltime-tomography (e.g. Chavent et al., 1994) and methods explicitly enforcing velocity-reflectivity consistency at the wave-equation level (Yang et al., 2021), or within an augmented objective function (Valensi and Baina, 2021). This cheap domain transformation makes it possible to passively update impedance during  $V_p$ -inversion, as opposed to reconstructing it by  $I_p$ WI at each iteration, with huge computational savings, especially in 3D.

This case study is the first published 3D field data application of GSOT to reflection-based FWI. The conclusions of Pladys et al. (2022) about the robustness of the objective function are confirmed by this work, and extended to reflection data fitting. The presence

of reflections in both the predicted and observed data since the first iteration (thanks to the reconstructed  $I_p$ ) is an ideal characteristic for GSOT (and, in general, objective functions sensitive to time-shifts), whereby the calculated data can be thought of as a shifted version of the observations through velocity-driven differences in move-out. Optimal transport, in this context, works in conjunction with the pseudotime re-parametrization to avert phase ambiguity respectively at mid-to-long and short offsets (Provenzano et al., 2023).

Each JFWI gradient computation requires 6 wavefield modellings, against 3 in time-domain FWI, thus being twice as expensive. It is worth pointing out that this is the price to pay for the time saved in building an accurate travelttime-based initial model, since the proposed methodology may start from very non-informative starting models and does not require phase identification and picking, aside from simple windowing and weighting.

The additional cost of GSOT is in the order of +30% at the frequency band used in this work (2.5-5 Hz). As described in Métivier et al. (2019) and observed by Pladys et al. (2022), the cost of computing optimal transport in the graph-space scales with the 3rd power of frequency, while the computational complexity of the finite-difference acoustic modelling varies with the 4th power of frequency. Therefore, the extra-cost than the  $L^2$ -norm becomes proportionally smaller as we move up in frequency in multi-scale inversion schemes (Bunks et al., 1995).

Though theoretically capable of ensuring convexity with respect to time shifts, GSOT does not altogether free waveform-inversion from cycle-skipping, and the recent literature on the subject (e.g., Górszczyk et al., 2021; Pladys et al., 2022) confirms that offset selection remains necessary to ensure convergence. Large values of expected time-shift  $\Delta t$  lead

to better-behaved objective function with respect traveltime differences, with larger valleys of attraction towards the global minimum, but at the same time make the objective function flatter (Métivier et al., 2019). The reason is that the larger  $\Delta t$ , the larger the importance of small amplitude events in the seismogram is in determining the optimal transport plan (Métivier and Brossier, 2021), which may dramatically collapse to a flat objective function, especially in noise-contaminated data. Hence the difficulty of ensuring convergence inverting for arrivals with very large traveltime differences with respect to the dominant period. In practice, the user has to perform a preliminary comparison between synthetic and observed data, from which expected maximum time-lags ( $\Delta T$ ) for GSOT may be chosen and tested.

With this in mind, it is worth pointing out that the integration of GSOT in JFWI considers the possibility to independently define reflection- $\Delta t$  and diving- $\Delta t$ , whereby an educated choice can be made based on the maximum expected time-shifts in the two propagation regimes in an otherwise rather user-independent inversion strategy. Along with the GSOT parameter-tuning, the definition of offset-windows and the separation between diving and reflection regimes, however, remain key manual/semi-automatic tasks of the workflow.

## CONCLUSIONS

Starting from a highly non-informative kinematic model that would expose the non linearity and limited wavenumber sensitivity of conventional FWI, a novel velocity model building methodology is applied to an OBC dataset from the North Sea. The proposed approach jointly inverts diving and reflected waves (JFWI) in a reflective starting model

using a graph-space optimal transport (GSOT) objective function in pseudotime. Minimal pre-processing is required, and the inverted dataset contains multiples, ghosts and elastic effects.

Preliminarily to GSOT JFWI, early-arrivals GSOT FWI is run on the very-short offset, followed by impedance-model building using a novel asymptotic-based preconditioner that significantly speeds-up the reflective model building. GSOT JFWI is then run in three widening-offset stages to build a suitable starting model for FWI. The JFWI+FWI results confirm the potential of GSOT in reducing cycle-skipping and the effectiveness of JFWI in exploiting jointly diving waves and reflections to obtain deep velocity updates while constraining the shallow subsurface.

The efficiency of the methodology is ensured by the pseudotime approach, that greatly reduces the need to iteratively reconstruct the reflectivity as kinematics is updated. Encouraging data prediction and sonic log reconstruction vouch for the effectiveness of the method in complementing the FWI wavenumber sensitivity at depth and mitigating its liability to cycle skipping, thus making it more independent from the quality of the traveltime-based starting model.

The results obtained in this challenging real-data exercise suggest that the proposed methodology may bring about improvements to current high-resolution velocity model building workflows, enriching the value of full-waveform methods in providing geologically plausible updates in conjunction with kinematics-based methods. Future work will focus on extending JFWI to the estimation of the anisotropic parameters, which in this work have been kept fixed to the ones derived from the traveltime-tomography model.

## **ACKNOWLEDGMENTS**

## REFERENCES

- Alkhalifah, T., 1997, Velocity analysis using nonhyperbolic moveout in transversely isotropic media: *Geophysics*, **62**, 1839–1854.
- Becache, E., S. Fauqueux, and P. Joly, 2003, Stability of Perfectly Matched Layers, Group Velocities and Anisotropic Waves: *Journal of Computational Physics*, **188**, 399–433.
- Becache, E., D. Givoli, and T. Hagstrom, 2010, High-order absorbing boundary conditions for anisotropic and convective wave equations: *Journal of Computational Physics*, **229**, 1099–1129.
- Bérenger, J.-P., 1994, A perfectly matched layer for absorption of electromagnetic waves: *Journal of Computational Physics*, **114**, 185–200.
- Beydoun, W. B., and A. Tarantola, 1988, First Born and Rytov approximation: Modeling and inversion conditions in a canonical example: *Journal of the Acoustical Society of America*, **83**, 1045–1055.
- Beylkin, G., 1985, Imaging of discontinuities in the inverse scattering problem by inversion of a causal generalized Radon transform: *Journal of Mathematical Physics*, **26**, 99–108.
- Blanch, J., J. O. A. Robertson, and W. W. Symes, 1995, Modeling of a constant Q: Methodology and algorithm for an efficient and optimally inexpensive viscoelastic technique: *Geophysics*, **60**, 176–184.
- Brossier, R., S. Operto, and J. Virieux, 2009, 2D elastic frequency-domain full-waveform inversion for imaging complex onshore structures: 71<sup>th</sup> Annual EAGE Conference & Exhibition, Amsterdam, Expanded Abstracts, EAGE, U019.
- , 2015, Velocity model building from seismic reflection data by full waveform inver-

- sion: *Geophysical Prospecting*, **63**, no. 2, 354–367.
- Bunks, C., F. M. Salek, S. Zaleski, and G. Chavent, 1995, Multiscale seismic waveform inversion: *Geophysics*, **60**, 1457–1473.
- Cerjan, C., D. Kosloff, R. Kosloff, and M. Reshef, 1985, A nonreflecting boundary condition for discrete acoustic and elastic wave equations: *Geophysics*, **50**, 2117–2131.
- Chavent, G., F. Clément, and S. Gómez, 1994, Automatic determination of velocities via migration-based travelttime waveform inversion: A synthetic data example: *SEG Technical Program Expanded Abstracts 1994*, 1179–1182.
- Dagnino, D., V. Sallarès, B. Biescas, and C. R. Ranero, 2016, Fine-scale thermohaline ocean structure retrieved with 2-d prestack full-waveform inversion of multichannel seismic data: Application to the gulf of cadiz (sw iberia): *Journal of Geophysical Research: Oceans*, **121**, 5452–5469.
- Davy, R. G., J. V. Morgan, T. A. Minshull, G. Bayrakci, J. M. Bull, D. Klaeschen, T. J. Reston, D. S. Sawyer, G. Lymer, and D. Cresswell, 2017, Resolving the fine-scale velocity structure of continental hyperextension at the Deep Galicia Margin using full-waveform inversion: *Geophysical Journal International*, **212**, 244–263.
- Farshad, M., and H. Chauris, 2021, Accelerating the multi-parameter least-squares reverse time migration using an appropriate preconditioner: *Computational Geosciences*, **25**, 2071–2092.
- Fichtner, A., and A. Villaseñor, 2015, Crust and upper mantle of the western mediterranean – constraints from full-waveform inversion: *Earth and Planetary Science Letters*, **428**, 52 – 62.
- Gholami, Y., R. Brossier, S. Operto, V. Prioux, A. Ribodetti, and J. Virieux, 2013, Which

- parametrization is suitable for acoustic VTI full waveform inversion? - Part 2: application to Valhall: *Geophysics*, **78**, R107–R124.
- Górszczyk, A., R. Brossier, and L. Métivier, 2021, Graph-space optimal transport concept for time-domain full-waveform inversion of ocean-bottom seismometer data: Nankai trough velocity structure reconstructed from a 1d model: *Journal of Geophysical Research: Solid Earth*, **126**, e2020JB021504.
- Guasch, L., O. C. Agudo, M.-X. Tang, P. Nachev, and M. Warner, 2020, Full-waveform inversion imaging of the human brain: *NPJ digital medicine*, **3**, 1–12.
- Hicks, E., H. Hoerber, M. Houbiers, S. P. Lescoffit, A. Ratcliffe, and V. Vinje, 2016, Time-lapse full-waveform inversion as a reservoir-monitoring tool – A North Sea case study: *The Leading Edge*, **35**, 850–858.
- Hicks, G. J., 2002, Arbitrary source and receiver positioning in finite-difference schemes using Kaiser windowed sinc functions: *Geophysics*, **67**, 156–166.
- Hicks, G. J., and R. G. Pratt, 2001, Reflection waveform inversion using local descent methods: estimating attenuation and velocity over a gas-sand deposit: *Geophysics*, **66**, 598–612.
- Huang, Y., and G. Schuster, 2014, Resolution limits for wave equation imaging: *Journal of Applied Geophysics*, **107**, 137–148.
- Irnaka, T. M., R. Brossier, L. Metivier, T. Bohlen, and Y. Pan, 2022, 3D Multi-component Full Waveform Inversion for Shallow-Seismic Target: Ettlingen Line Case Study: *Geophysical Journal International*, **229**, 1017–1040.
- Jannane, M., W. Beydoun, E. Crase, D. Cao, Z. Koren, E. Landa, M. Mendes, A. Pica, M. Noble, G. Roeth, S. Singh, R. Snieder, A. Tarantola, and D. Trezeguet, 1989, Wave-

- lengths of Earth structures that can be resolved from seismic reflection data: *Geophysics*, **54**, 906–910.
- Kamath, N., R. Brossier, L. Métivier, A. Pladys, and P. Yang, 2021, Multiparameter full-waveform inversion of 3D ocean-bottom cable data from the Valhall field: *Geophysics*, **86**, B15–B35.
- Kantorovich, L., 1942, On the transfer of masses: *Dokl. Acad. Nauk. USSR*, **37**, 7–8.
- Keating, S. D., and K. A. Innanen, 2021, Null-space shuttles for targeted uncertainty analysis in full-waveform inversion: *Geophysics*, **86**, R63–R76.
- Lailly, P., 1983, The seismic problem as a sequence of before-stack migrations: Presented at the Conference on Inverse Scattering: Theory and Applications, SIAM, Philadelphia.
- Li, Y., R. Brossier, and L. Métivier, 2019, Joint FWI for imaging deep structures: A graph-space OT approach: *SEG Technical Program Expanded Abstracts 2019*, 1290–1294.
- Li, Y., and H. Chauris, 2018, Coupling direct inversion to common-shot image-domain velocity analysis: *Geophysics*, **83**, R497–R514.
- Marty, P., C. Boehm, and A. Fichtner, 2021, Acoustoelastic full-waveform inversion for transcranial ultrasound computed tomography: *Medical Imaging 2021: Ultrasonic Imaging and Tomography*, International Society for Optics and Photonics, 1160211.
- Métivier, L., and R. Brossier, 2016, The SEISCOPE optimization toolbox: A large-scale nonlinear optimization library based on reverse communication: *Geophysics*, **81**, F11–F25.
- , 2021, New insights on the graph space optimal transport distance for full waveform inversion: Presented at the SEG Technical Program Expanded Abstracts 2021.
- Métivier, L., R. Brossier, Q. Mérigot, and E. Oudet, 2019, A graph space optimal transport

- distance as a generalization of  $L^p$  distances: application to a seismic imaging inverse problem: *Inverse Problems*, **35**, 085001.
- Mora, P. R., 1989, Inversion = migration + tomography: *Geophysics*, **54**, 1575–1586.
- Nocedal, J., 1980, Updating Quasi-Newton Matrices With Limited Storage: *Mathematics of Computation*, **35**, 773–782.
- Operto, S., R. Brossier, Y. Gholami, L. Métivier, V. Prieux, A. Ribodetti, and J. Virieux, 2013, A guided tour of multiparameter full waveform inversion for multicomponent data: from theory to practice: *The Leading Edge*, **Special section Full Waveform Inversion**, 1040–1054.
- Operto, S., and A. Miniussi, 2018, On the role of density and attenuation in 3D multiparameter visco-acoustic VTI frequency-domain FWI: an OBC case study from the North Sea: *Geophysical Journal International*, **213**, 2037–2059.
- Operto, S., A. Miniussi, R. Brossier, L. Combe, L. Métivier, V. Monteiller, A. Ribodetti, and J. Virieux, 2015, Efficient 3-D frequency-domain mono-parameter full-waveform inversion of ocean-bottom cable data: application to Valhall in the visco-acoustic vertical transverse isotropic approximation: *Geophysical Journal International*, **202**, 1362–1391.
- Pladys, A., R. Brossier, N. Kamath, and L. Métivier, 2022, Robust FWI with graph space optimal transport: application to 3D OBC Valhall data: *Geophysics*, **87**, 1–76.
- Plessix, R. E., 2013, A pseudo-time formulation for acoustic full waveform inversion: *Geophysical Journal International*, **192**, 613–630.
- Pratt, R. G., 1999, Seismic waveform inversion in the frequency domain, part I: theory and verification in a physical scale model: *Geophysics*, **64**, 888–901.
- Pratt, R. G., and R. M. Shipp, 1999, Seismic waveform inversion in the frequency domain,

- part II: Fault delineation in sediments using crosshole data: *Geophysics*, **64**, 902–914.
- Pratt, R. G., L. Sirgue, B. Hornby, and J. Wolfe, 2008, Cross-well waveform tomography in fine-layered sediments - meeting the challenges of anisotropy: 70<sup>th</sup> Annual International Meeting, EAGE, 70<sup>th</sup> Annual EAGE Conference & Exhibition, Roma, F020.
- Prieux, V., R. Brossier, Y. Gholami, S. Operto, J. Virieux, O. Barkved, and J. Kommedal, 2011, On the footprint of anisotropy on isotropic full waveform inversion: the Valhall case study: *Geophysical Journal International*, **187**, 1495–1515.
- Provenzano, G., R. Brossier, and L. Métivier, 2023, Robust and efficient waveform-based velocity-model building by optimal transport in the pseudotime domain: *Methodology: Geophysics*, **88**, U49–U70.
- Provenzano, G., M. E. Vardy, and T. J. Henstock, 2018, Decimetric-resolution stochastic inversion of shallow marine seismic reflection data: dedicated strategy and application to a geohazard case study: *Geophysical Journal International*, **214**, 1683–1700.
- Qin, B., T. Allemand, and G. Lambaré, 2015, Full waveform inversion using preserved amplitude reverse time migration: *SEG Technical Program Expanded Abstracts 2015*, 1252–1257.
- Ray, A., A. Sekar, G. M. Hoversten, and U. Albertin, 2016, Frequency domain full waveform elastic inversion of marine seismic data from the alba field using a bayesian trans-dimensional algorithm: *Geophysical Journal International*, **205**, 915–937.
- Rickett, J., and P. Childs, 2011, Full-waveform inversion in the travelttime domain.
- Robertson, J. O. A., K. Holliger, A. G. Green, A. Pugin, and R. D. Iaco, 1996, Effects of near-surface waveguides on shallow high-resolution seismic refraction and reflection data: *Geophysical Research Letters*, **23**, 495–498.

- Sambridge, M., and K. Mosegaard, 2002, Monte Carlo methods in geophysical inverse problems: *Reviews of Geophysics*, **40**, 1–29.
- Schleicher, J., C. J.C., and N. A., 2008, A comparison of imaging conditions for wave-equation shot-profile migration: *Geophysics*, **73**, S219–S227.
- Sirgue, L., O. I. Barkved, J. Dellinger, J. Etgen, U. Albertin, and J. H. Kommedal, 2010, Full waveform inversion: the next leap forward in imaging at Valhall: *First Break*, **28**, 65–70.
- Tarantola, A., 1984, Inversion of seismic reflection data in the acoustic approximation: *Geophysics*, **49**, 1259–1266.
- , 1986, A strategy for non linear inversion of seismic reflection data: *Geophysics*, **51**, 1893–1903.
- Thomsen, L. A., 1986, Weak elastic anisotropy: *Geophysics*, **51**, 1954–1966.
- Thurin, J., R. Brossier, and L. Métivier, 2019, Ensemble-based uncertainty estimation in full waveform inversion: *Geophysical Journal International*, **219**, 1613–1635.
- Valensi, R., and R. Baina, 2021, A time consistent waveform inversion (twin) method: Presented at the 82nd EAGE Annual Conference & Exhibition.
- Virieux, J., and S. Operto, 2009, An overview of full waveform inversion in exploration geophysics: *Geophysics*, **74**, WCC1–WCC26.
- Woodward, M. J., 1992, Wave-equation tomography: *Geophysics*, **57**, 15–26.
- Xu, S., D. Wang, F. Chen, G. Lambaré, and Y. Zhang, 2012, Inversion on reflected seismic wave: SEG Technical Program Expanded Abstracts 2012, 1–7.
- Yang, P., R. Brossier, L. Métivier, and J. Virieux, 2016a, A review on the systematic formulation of 3D multiparameter full waveform inversion in viscoelastic medium: *Geo-*

- physical Journal International, **207**, 129–149.
- , 2016b, Wavefield reconstruction in attenuating media: A checkpointing-assisted reverse-forward simulation method: *Geophysics*, **81**, R349–R362.
- Yang, P., R. Brossier, L. Métivier, J. Virieux, and W. Zhou, 2018, A Time-Domain Preconditioned Truncated Newton Approach to Multiparameter Visco-acoustic Full Waveform Inversion: *SIAM Journal on Scientific Computing*, **40**, B1101–B1130.
- Yang, Y., J. Ramos-Martinez, D. Whitmore, G. Huang, and N. Chemingui, 2021, Simultaneous velocity and reflectivity inversion: Fwi+ lsrtm: Presented at the 82nd EAGE Annual Conference & Exhibition.
- Yao, G., D. Wu, and S. Wang, 2020, A review on reflection waveform inversion: *Petroleum science*, **17**, 334–351.
- Yong, P., R. Brossier, and L. Métivier, 2022, Parsimonious truncated newton method for time-domain full-waveform inversion based on the fourier-domain full-scattered-field approximation: *Geophysics*, **87**, R123–R146.
- Zhang, X., and A. Curtis, 2020, Variational full-waveform inversion: *Geophysical Journal International*, **222**, 406–411.
- Zhou, W., R. Brossier, S. Operto, and J. Virieux, 2015, Full waveform inversion of diving & reflected waves for velocity model building with impedance inversion based on scale separation: *Geophysical Journal International*, **202**, 1535–1554.
- Zhou, W., R. Brossier, S. Operto, J. Virieux, and P. Yang, 2018, Velocity model building by waveform inversion of early arrivals and reflections: a 2d ocean-bottom-cable study with gas cloud effects: *Geophysics*, **83(2)**, R141–R157.

## LIST OF FIGURES

1	Acquisition geometry overlaid to the horizontal slice at 1.1 km depth to show the low-velocity cloud position (Kamath et al., 2021): receiver cables (blue), shot positions (white), projection of well-logs location at the surface, control receiver cables (Rec. A and B) used for QC. . . . .	49
2	Estimated wavelet in the 2.5-5 Hz band (a) and data windows on an example shot gather proximal to the LVZ, for: a) source estimation, b) $I_p$ WI, c) reflection $W_r$ and d) refraction $W_e$ in the JFWI objective function (equation 1) . . . . .	50
3	Starting $\eta$ model: the anisotropic parameters are part of the tomographic model by AkerBP; as well as the constant attenuation, they are used in modelling, but kept constant during inversion. The bottom 4 panels are vertical slices cutting through the volume, while the greyscale ones are horizontal slices at constant depth (0.2, 0.5 and 1.1 km). Slices locations are indicated by the letter-coded black lines. . . . .	51
4	<b>Starting 1D <math>V_p</math> model.</b> Density is derived from this $V_p$ model using a Gardner’s law relationship, hence initial $I_p$ is also smooth and linearly increasing. The bottom 4 panels are vertical slices cutting through the volume, while the greyscale ones are horizontal slices at constant depth (0.2, 0.5 and 1.1 km). Slices locations are indicated by the letter-coded black lines. . . . .	52
5	<b>Early-wave FWI offset window 1:</b> 5 Hz GSOT diving wave FWI results, offsets < 4.8 km, starting from the initial 1D model in Figure 4. The bottom 4 panels are vertical slices cutting through the volume, while the greyscale ones are horizontal slices at constant depth (0.2, 0.5 and 1.1 km). Slices locations are indicated by the letter-coded black lines. . . . .	53
6	Speed-up in misfit reduction of proposed asymptotic preconditioner (deconvolution imaging condition in time-domain) vs wavefield illumination compensation. . . . .	54
7	Density perturbation obtained after $I_p$ WI using a) proposed asymptotic preconditioner (deconvolution imaging condition in time-domain) and b) wavefield illumination compensation on a two-dimensional line extracted along cable A, close to the LVZ (Figure 1) . . . . .	55
8	<b>JFWI offset window 2:</b> 5 Hz Pseudotime GSOT JFWI results, offsets < 7 km. The bottom 4 panels are vertical slices cutting through the volume, while the greyscale ones are horizontal slices at constant depth (0.2, 0.5 and 1.1 km). Slices locations are indicated by the letter-coded black lines. . . . .	56

- 9    **JFWI offset window 4:** 5 Hz Pseudotime GSOT JFWI results, full offsets. The bottom 4 panels are vertical slices cutting through the volume, while the greyscale ones are horizontal slices at constant depth (0.2, 0.5 and 1.1 km). Slices locations are indicated by the letter-coded black lines. A vertical profile is extracted at the LVZ (red asterisk on horizontal slices), showing that the proposed workflow updates  $V_p$  consistently with the reference tomographic model despite the very simple starting model. . . . . 57
  
- 10   **Reference macromodel:** Reflection traveltime tomography model by AkerBP. The bottom 4 panels are vertical slices cutting through the volume, while the greyscale ones are horizontal slices at constant depth (0.2, 0.5 and 1.1 km). Slices locations are indicated by the letter-coded black lines. Note how the final JFWI in Figure 9, and in the vertical profile, identifies the position of the low-velocity areas and the regional velocity trends of the reference kinematics model starting from the 1D initial guess. . . . . 58
  
- 11   **FWI after JFWI:** 5 Hz Pseudotime GSOT JFWI + GSOT FWI results, full offsets. The bottom 4 panels are vertical slices cutting through the volume, while the greyscale ones are horizontal slices at constant depth (0.2, 0.5 and 1.1 km). Slices locations are indicated by the letter-coded black lines. Same vertical profile location as for Figure 9. . . . . 59
  
- 12   **Conventional FWI:** 5 Hz GSOT FWI results, full offsets stage after a 6-step data-domain layer-stripping workflow starting from the initial 1D model (Pladys et al., 2022). The bottom 4 panels are vertical slices cutting through the volume, while the greyscale ones are horizontal slices at constant depth (0.2, 0.5 and 1.1 km). Slices locations are indicated by the letter-coded black lines. Note, in particular in the vertical profile at the LVZ, that the JFWI+FWI and conventional FWI models are close down to 1.5 km depth, below which the JFWI contribution becomes apparent in escaping from the initial  $V_p$  trend. . . . . 60
  
- 13   **Data fit QC on common receiver gather close to the low-velocity cloud (cable A, Figure 1):** a) Initial, b) Initial after short-offset diving wave FWI and  $I_p$ WI; c) GSOT JFWI. Synthetic and observed data alternate in the greyscale image with a 15-trace interval. Fit improves as continuities of seismic events increases. On the left, selected wiggle traces at the positions indicated by the red vertical lines in the greyscale plot . . . . . 61
  
- 14   **Data fit QC on common receiver gather away from the low-velocity cloud (cable B, Figure 1):** a) Initial, b) Initial after short-offset diving wave FWI and  $I_p$ WI; c) GSOT JFWI. Synthetic and observed data alternate in the greyscale image with a 15-trace interval. Fit improves as continuities of seismic events increases. On the left, selected wiggle traces at the positions indicated by the red vertical lines in the greyscale plot . . . . . 62

15	Data fit QC on common shot gather close to the low-velocity cloud (cable A). Comparison between FWI starting from the JFWI model (a) and layer-stripping conventional FWI starting from initial model (Pladys et al., 2022) (b). . . . .	63
16	Data fit QC on common shot gather away from the low-velocity cloud (cable B). Comparison between FWI starting from the JFWI model (a) and layer-stripping conventional FWI starting from initial model (Pladys et al., 2022) (b). . . . .	64
17	Cross-correlation of field and predicted data with a, b) initial model, c, d) FWI starting from initial model, e, f) FWI starting from JFWI model . . . .	65
18	Cross-correlation of field and predicted data in the reflection window, with a, b) FWI starting from initial model, c, d) FWI starting from JFWI model .	66
19	Source estimation quality check. The stationarity of the source wavelets estimated on different shots, at different locations should improve as the model quality increases, i.e. as the estimated model approximates the true one. $L^2$ value refers to the variance of the estimate. Red line is the envelope of the average wavelet of each panel, white one is the envelope of the reference wavelet estimated on the short-offset early arrivals only for inversion. . . . .	67
20	Well log predictions by JFWI+FWI and FWI using GSOT. Log P-wave velocities are converted to time, low-pass filtered within half a period for the maximum modelling frequency (5 Hz), and converted back to depth. Logs positions are plotted over the 1 km depth slice in Figure 1 . . . . .	68
21	Correlation coefficient between low-pass filtered logs and inverted velocities at the same location. Note that, although in Log-2 FWI is closer to the ground-truth than JFWI (Figure 20), the correlation coefficient is larger for JFWI, probably resulting from a better prediction of the velocity changes with depth. . . . .	69
22	2D RTM CIG gathers along cable A at offsets between 0 and 6 km. a) Initial 1D model; b) FWI starting from the 1D model; c) JFWI+FWI starting from the 1D model; d) Reference tomography model by Aker BP. The upper x-axis indicates the position of the CIG along cable A. . . . .	70
23	RTM 2D images along cable A. a) Initial 1D model; b) FWI starting from the 1D model; c) JFWI+FWI starting from the 1D model; d) Reference tomography model by Aker BP . . . . .	71

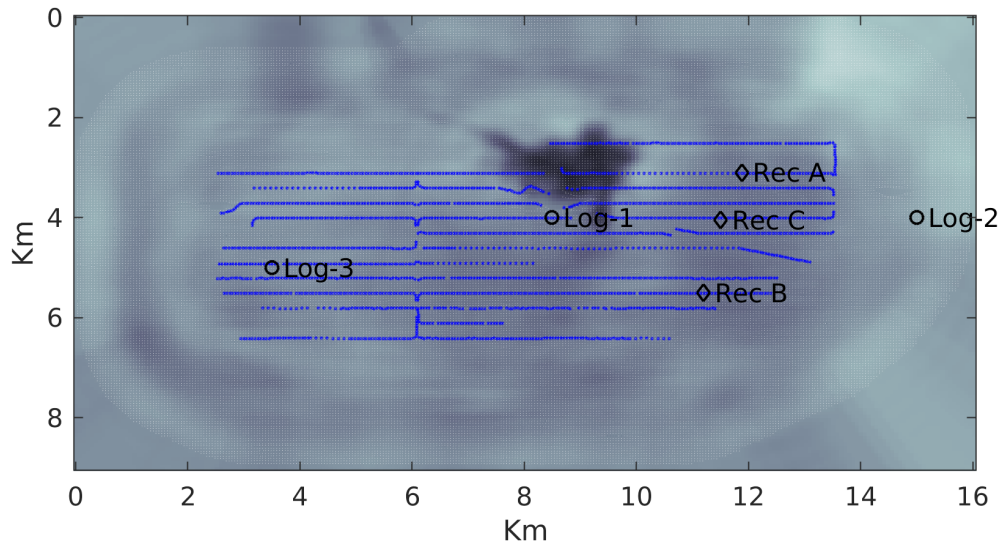


Figure 1: Acquisition geometry overlaid to the horizontal slice at 1.1 km depth to show the low-velocity cloud position (Kamath et al., 2021): receiver cables (blue), shot positions (white), projection of well-logs location at the surface, control receiver cables (Rec. A and B) used for QC.

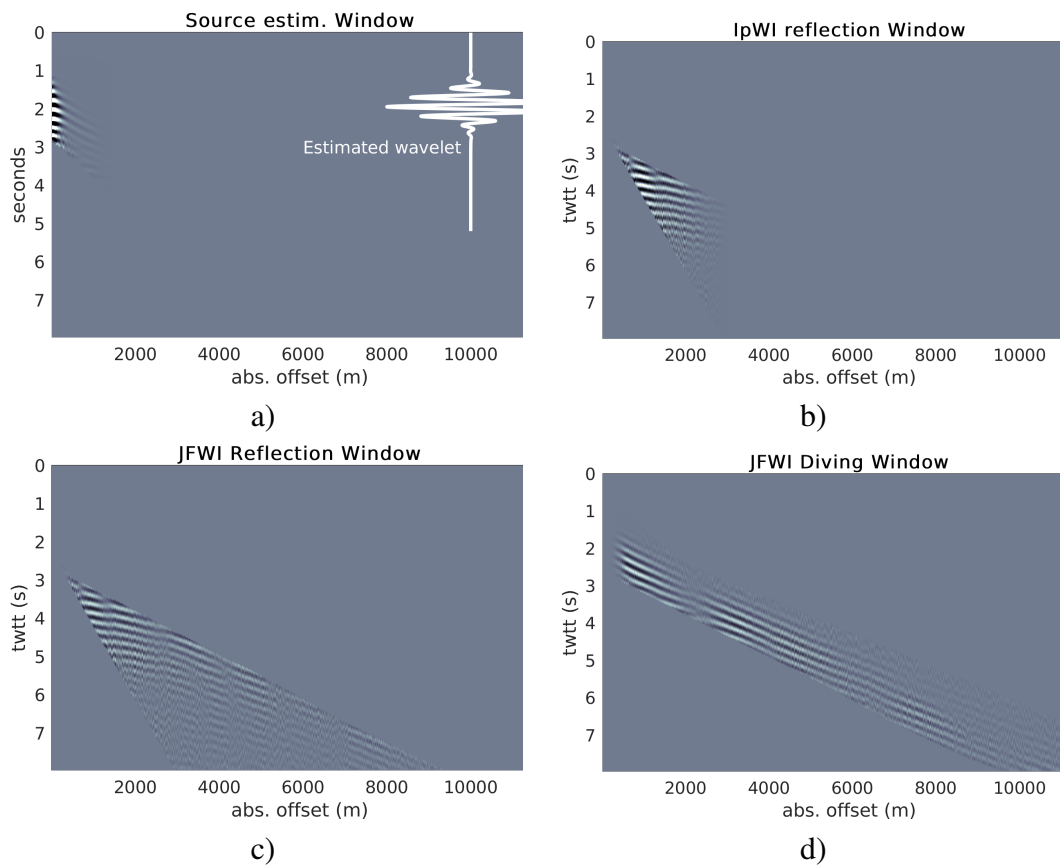


Figure 2: Estimated wavelet in the 2.5-5 Hz band (a) and data windows on an example shot gather proximal to the LVZ, for: a) source estimation, b)  $I_p$ WI, c) reflection  $W_r$  and d) refraction  $W_e$  in the JFWI objective function (equation 1)

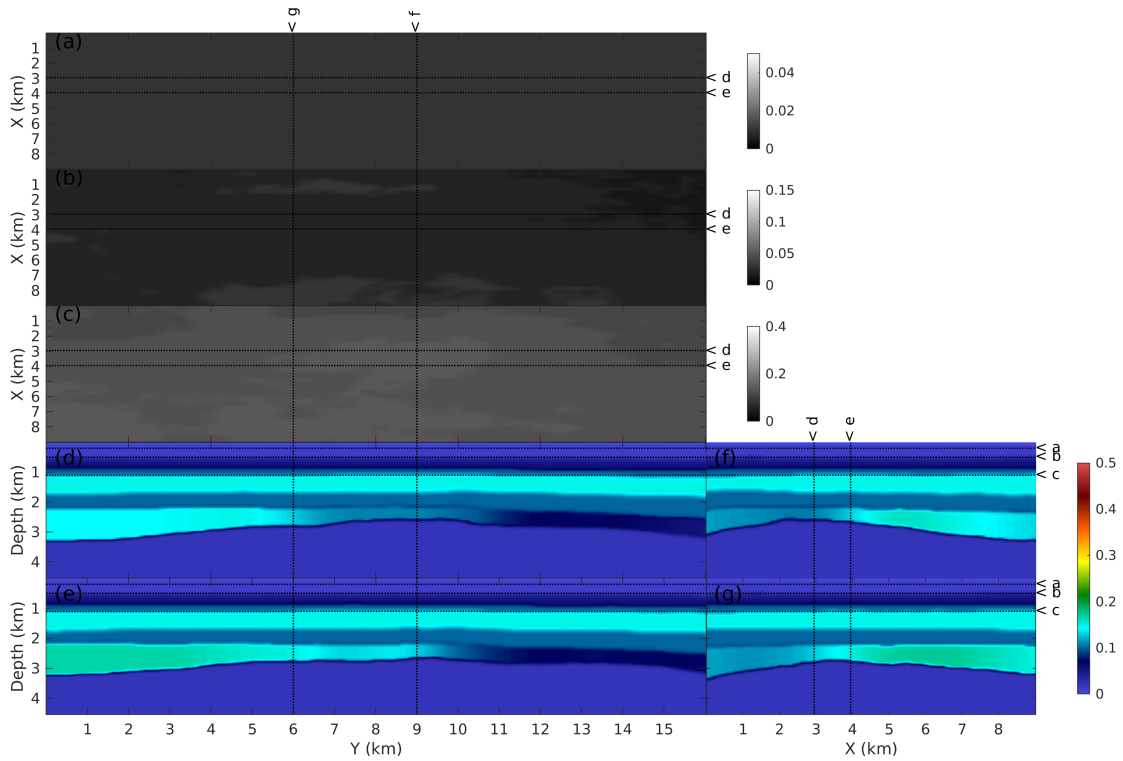


Figure 3: Starting  $\eta$  model: the anisotropic parameters are part of the tomographic model by AkerBP; as well as the constant attenuation, they are used in modelling, but kept constant during inversion. The bottom 4 panels are vertical slices cutting through the volume, while the greyscale ones are horizontal slices at constant depth (0.2, 0.5 and 1.1 km). Slices locations are indicated by the letter-coded black lines.

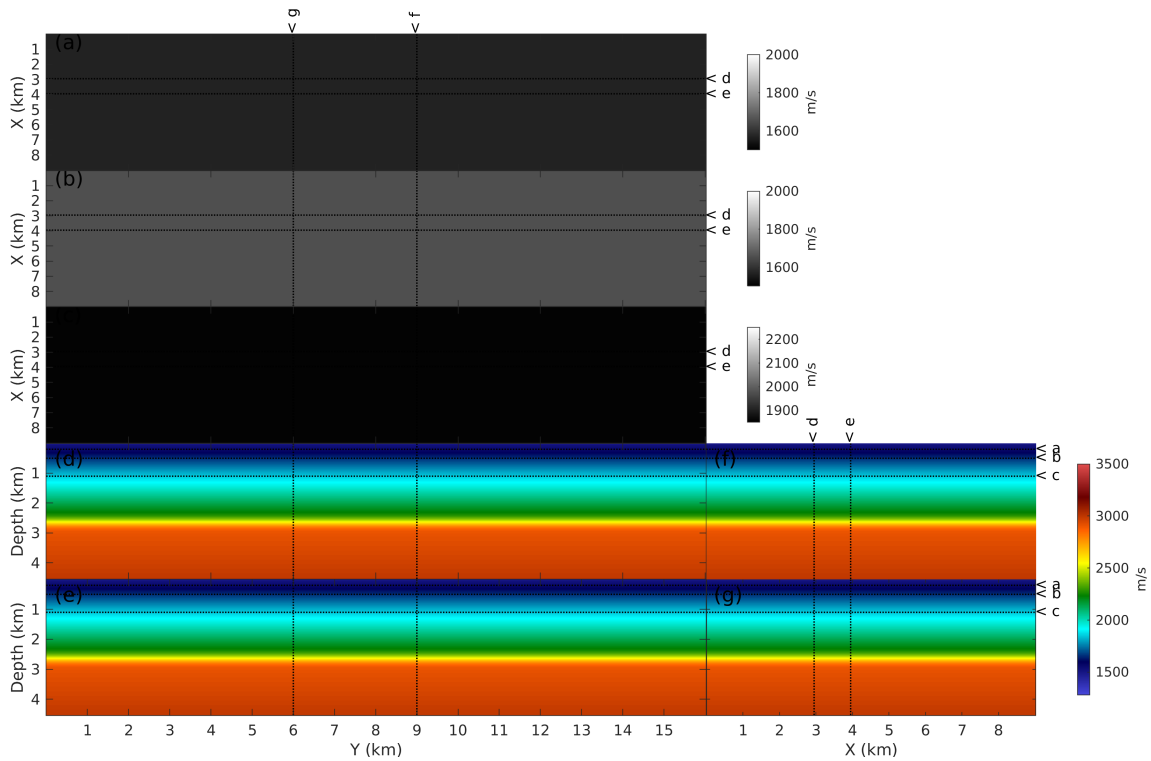


Figure 4: **Starting 1D  $V_p$  model.** Density is derived from this  $V_p$  model using a Gardner's law relationship, hence initial  $I_p$  is also smooth and linearly increasing. The bottom 4 panels are vertical slices cutting through the volume, while the greyscale ones are horizontal slices at constant depth (0.2, 0.5 and 1.1 km). Slices locations are indicated by the letter-coded black lines.

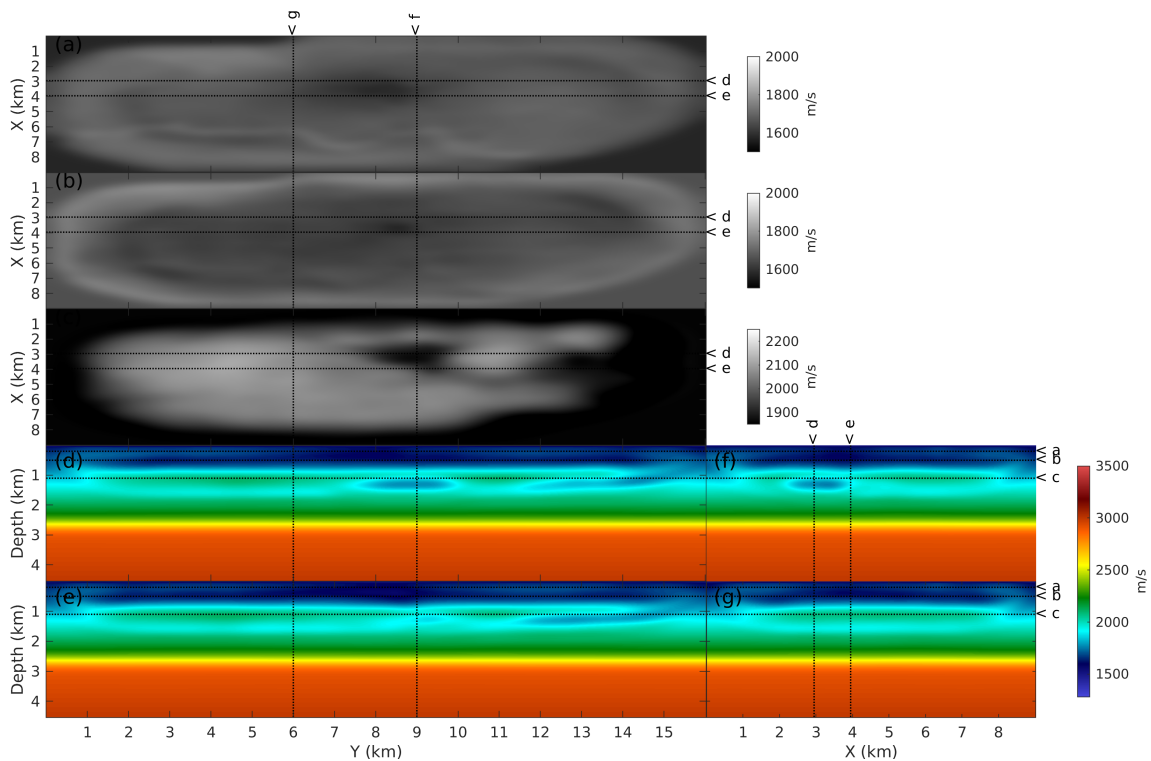


Figure 5: **Early-wave FWI offset window 1**: 5 Hz GSOT diving wave FWI results, offsets  $< 4.8$  km, starting from the initial 1D model in Figure 4. The bottom 4 panels are vertical slices cutting through the volume, while the greyscale ones are horizontal slices at constant depth (0.2, 0.5 and 1.1 km). Slices locations are indicated by the letter-coded black lines.

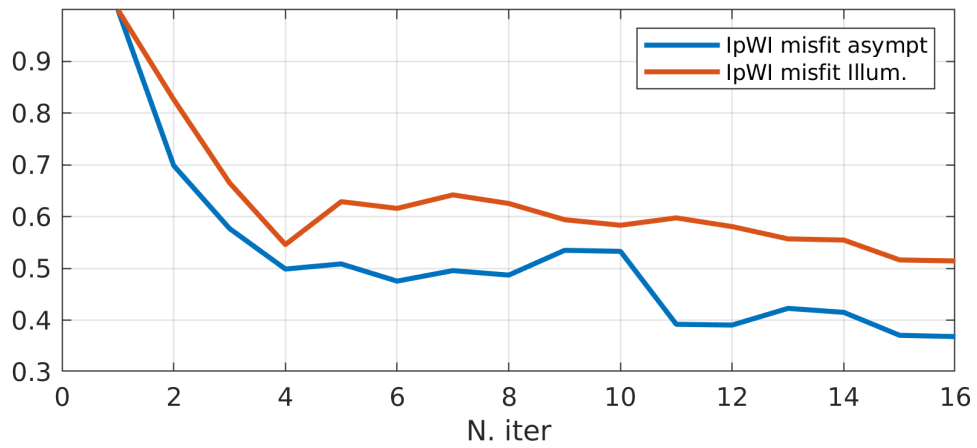


Figure 6: Speed-up in misfit reduction of proposed asymptotic preconditioner (deconvolution imaging condition in time-domain) vs wavefield illumination compensation.

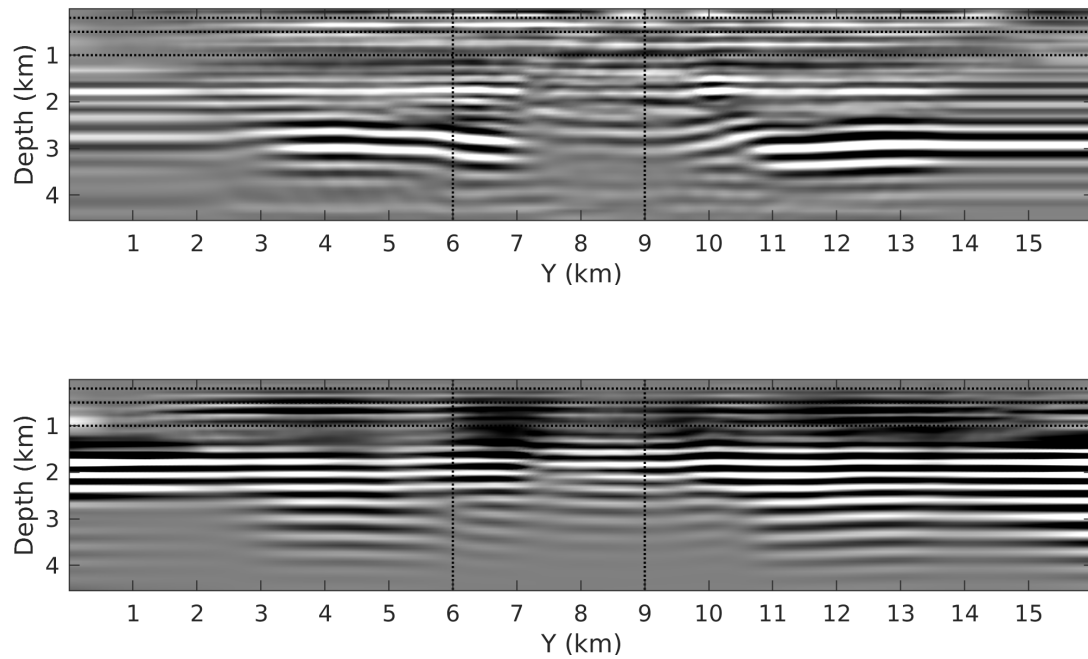


Figure 7: Density perturbation obtained after  $I_p$ WI using a) proposed asymptotic preconditioner (deconvolution imaging condition in time-domain) and b) wavefield illumination compensation on a two-dimensional line extracted along cable A, close to the LVZ (Figure 1)

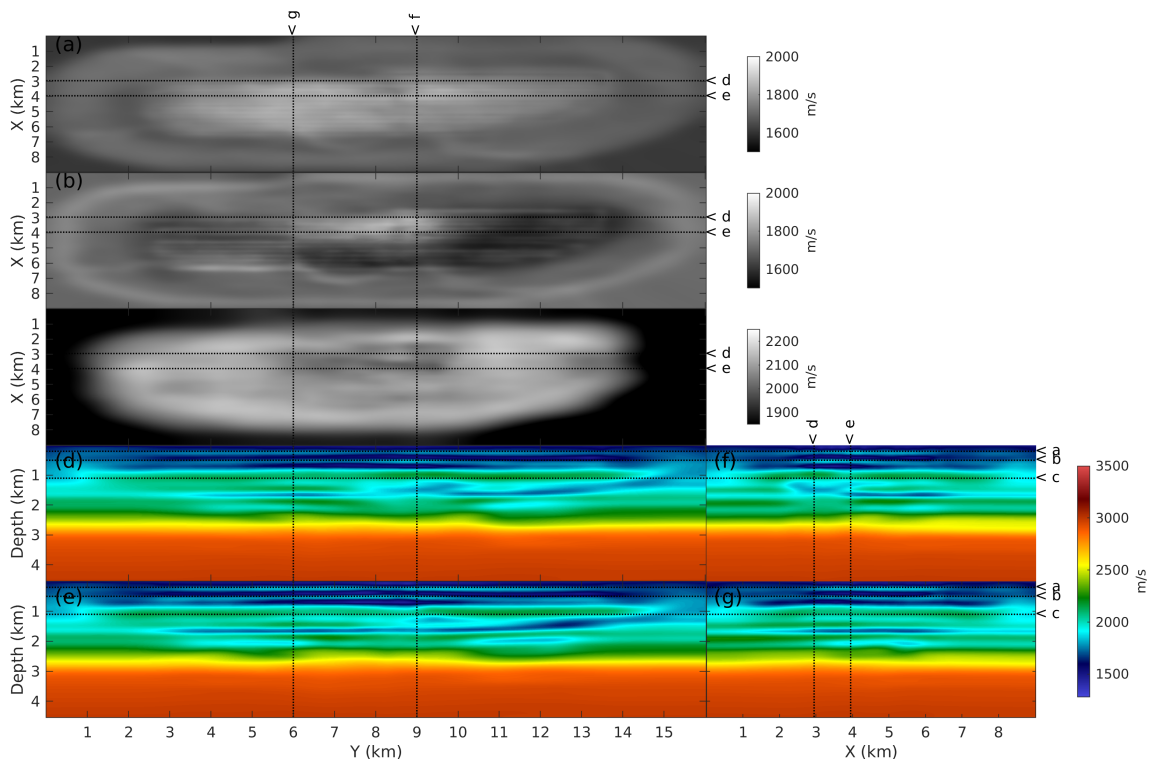


Figure 8: **JFWI offset window 2**: 5 Hz Pseudotime GSOT JFWI results, offsets < 7 km. The bottom 4 panels are vertical slices cutting through the volume, while the greyscale ones are horizontal slices at constant depth (0.2, 0.5 and 1.1 km). Slices locations are indicated by the letter-coded black lines.

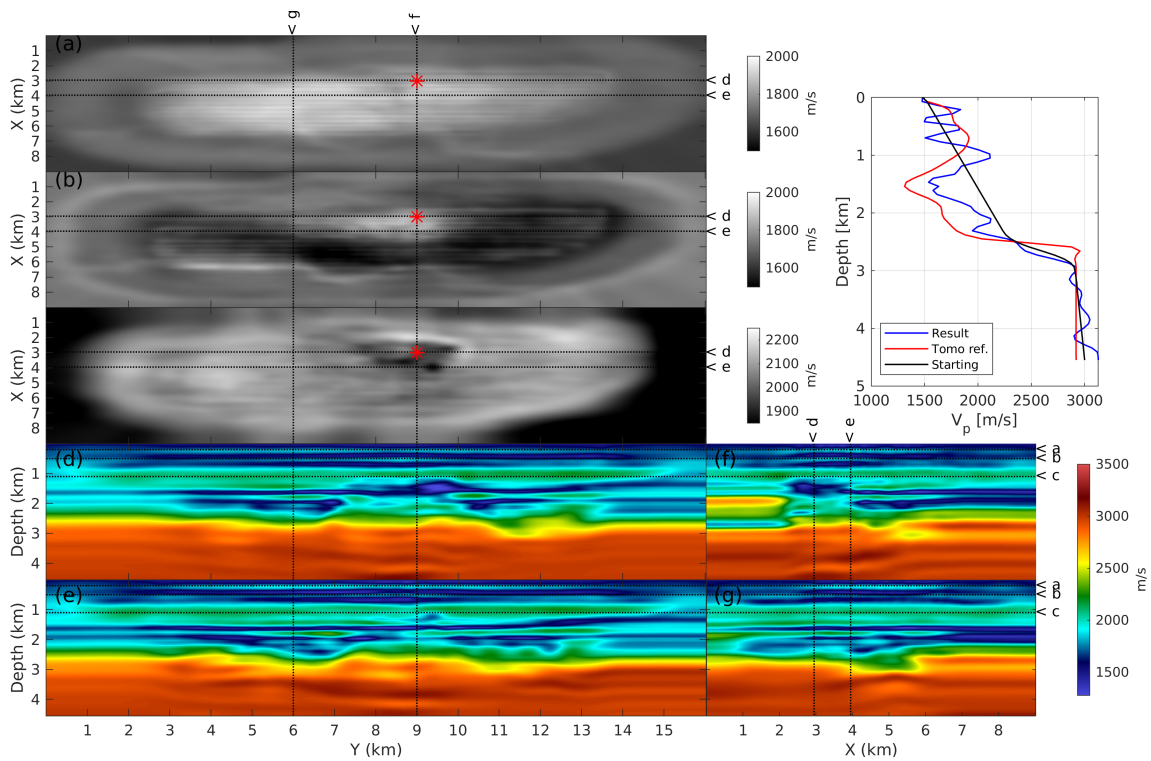


Figure 9: **JFWI offset window 4: 5 Hz Pseudotime GSOT JFWI results, full offsets.** The bottom 4 panels are vertical slices cutting through the volume, while the greyscale ones are horizontal slices at constant depth (0.2, 0.5 and 1.1 km). Slices locations are indicated by the letter-coded black lines. A vertical profile is extracted at the LVZ (red asterisk on horizontal slices), showing that the proposed workflow updates  $V_p$  consistently with the reference tomographic model despite the very simple starting model.

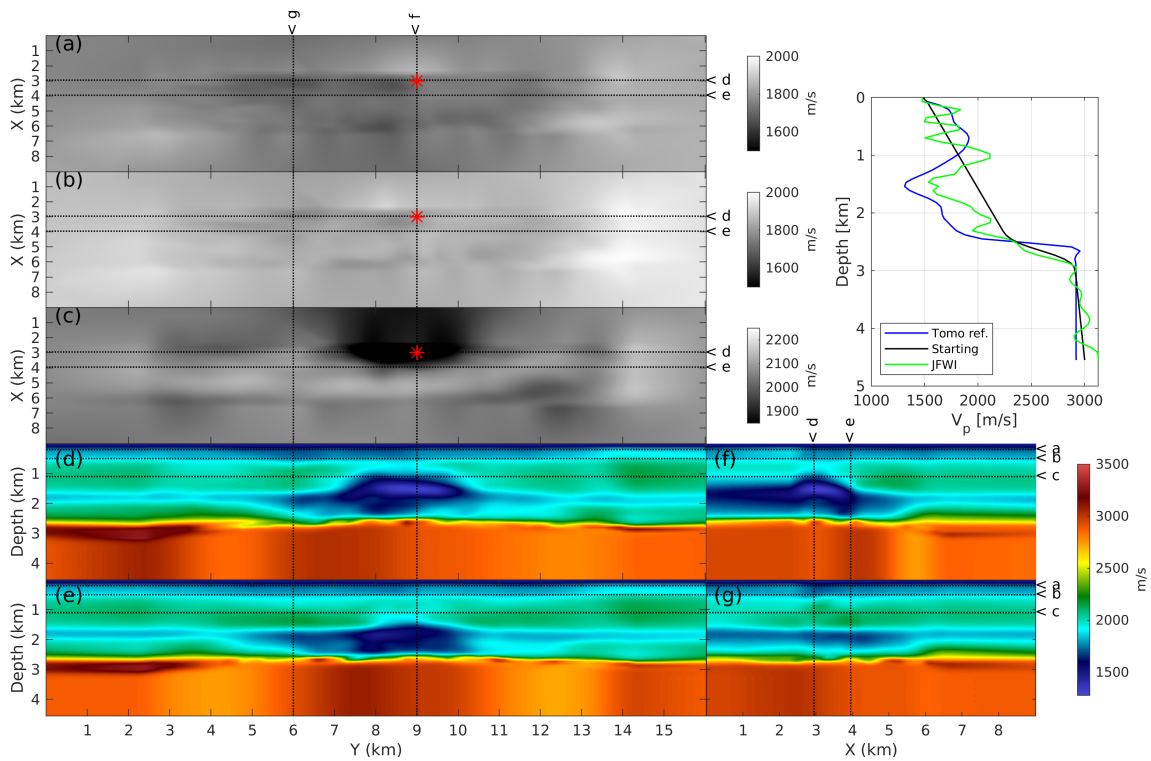


Figure 10: **Reference macromodel**: Reflection travelttime tomography model by AkerBP. The bottom 4 panels are vertical slices cutting through the volume, while the greyscale ones are horizontal slices at constant depth (0.2, 0.5 and 1.1 km). Slices locations are indicated by the letter-coded black lines. Note how the final JFWI in Figure 9, and in the vertical profile, identifies the position of the low-velocity areas and the regional velocity trends of the reference kinematics model starting from the 1D initial guess.

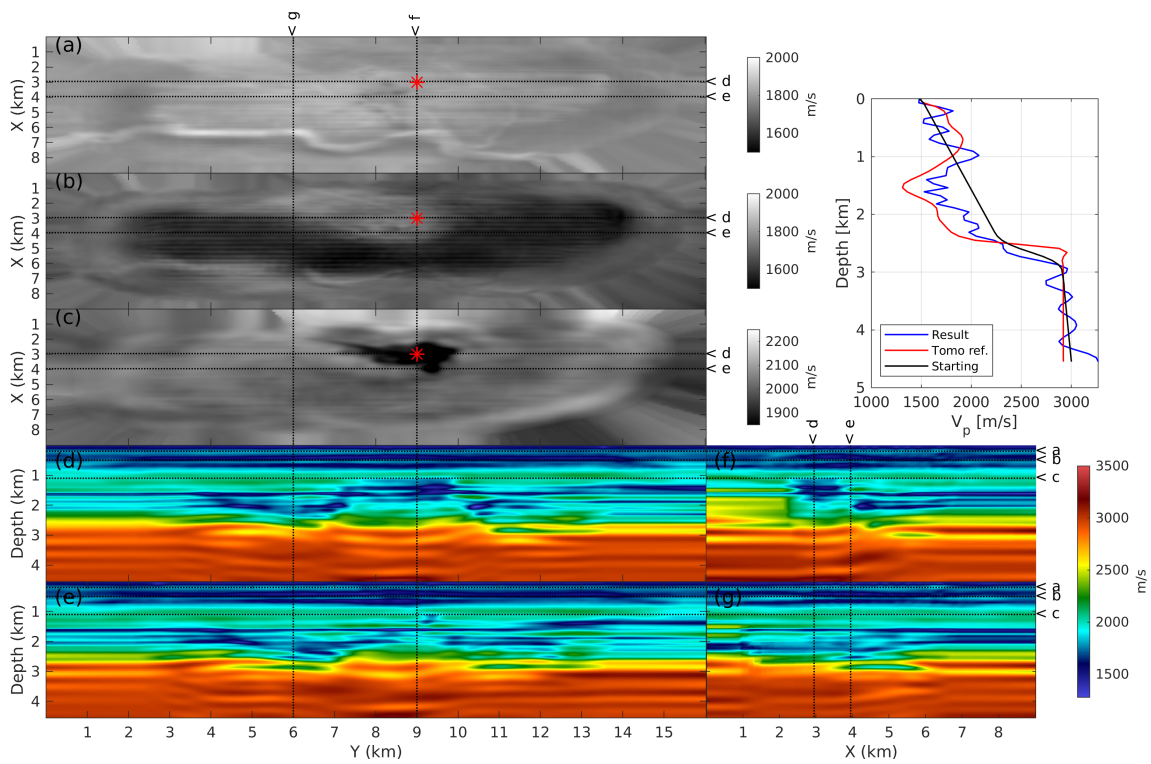


Figure 11: **FWI after JFWI**: 5 Hz Pseudotime GSOT JFWI + GSOT FWI results, full offsets. The bottom 4 panels are vertical slices cutting through the volume, while the greyscale ones are horizontal slices at constant depth (0.2, 0.5 and 1.1 km). Slices locations are indicated by the letter-coded black lines. Same vertical profile location as for Figure 9.

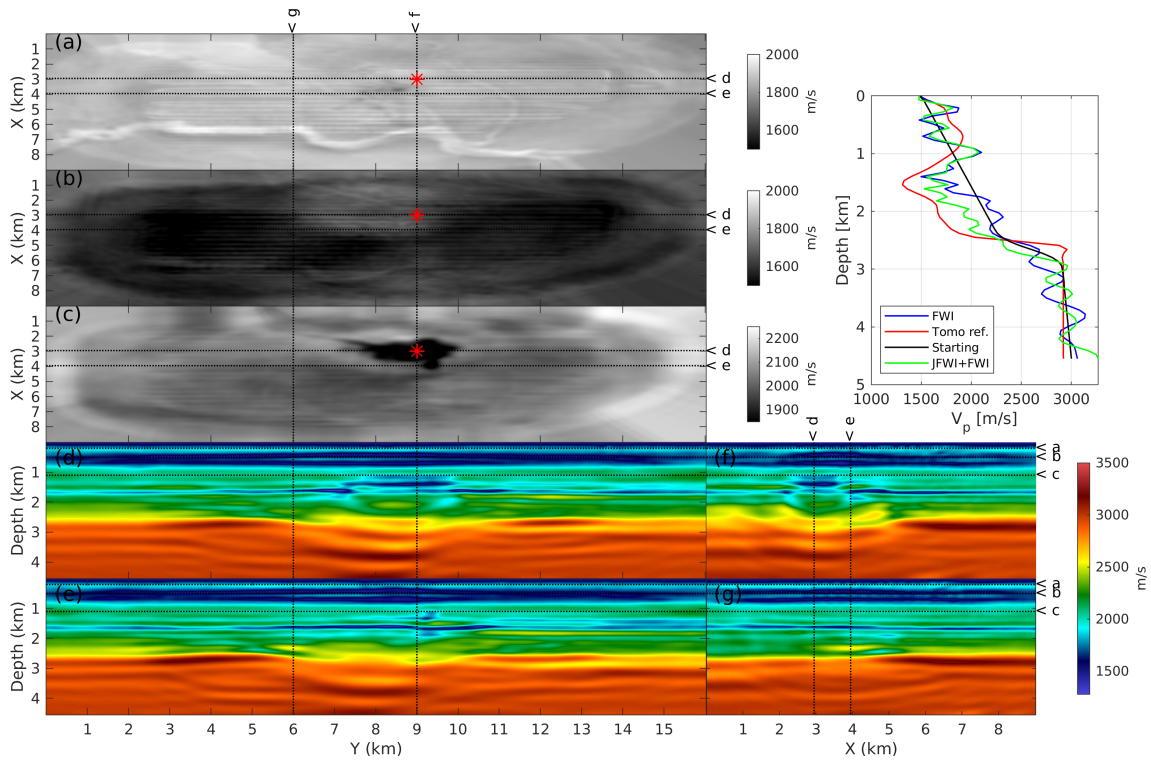


Figure 12: **Conventional FWI**: 5 Hz GSOT FWI results, full offsets stage after a 6-step data-domain layer-stripping workflow starting from the initial 1D model (Pladys et al., 2022). The bottom 4 panels are vertical slices cutting through the volume, while the greyscale ones are horizontal slices at constant depth (0.2, 0.5 and 1.1 km). Slices locations are indicated by the letter-coded black lines. Note, in particular in the vertical profile at the LVZ, that the JFWI+FWI and conventional FWI models are close down to 1.5 km depth, below which the JFWI contribution becomes apparent in escaping from the initial  $V_p$  trend.

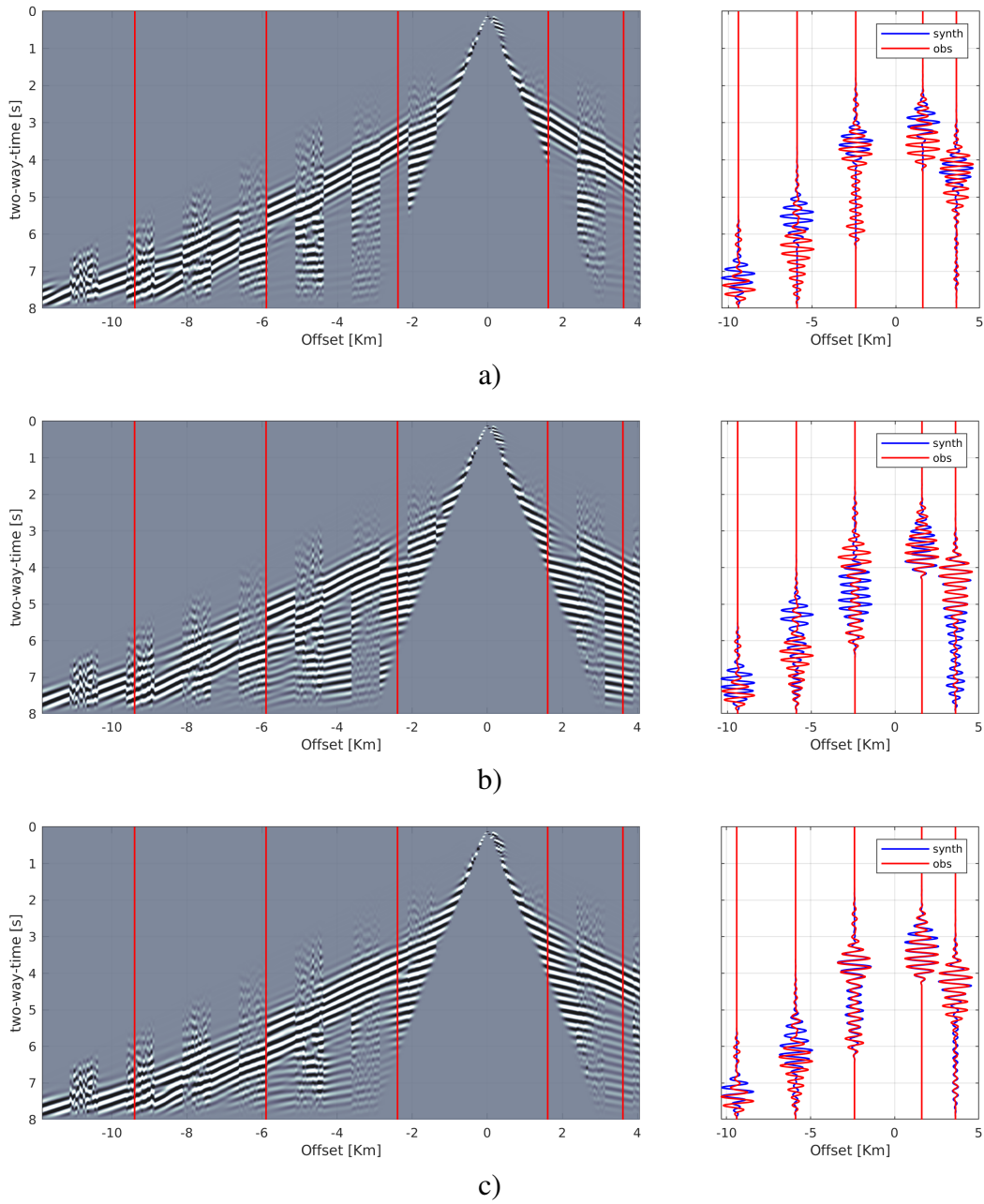


Figure 13: Data fit QC on common receiver gather close to the low-velocity cloud (cable A, Figure 1): a) Initial, b) Initial after short-offset diving wave FWI and  $I_p$  WI; c) GSOT JFWI. Synthetic and observed data alternate in the greyscale image with a 15-trace interval. Fit improves as continuities of seismic events increases. On the left, selected wiggle traces at the positions indicated by the red vertical lines in the greyscale plot

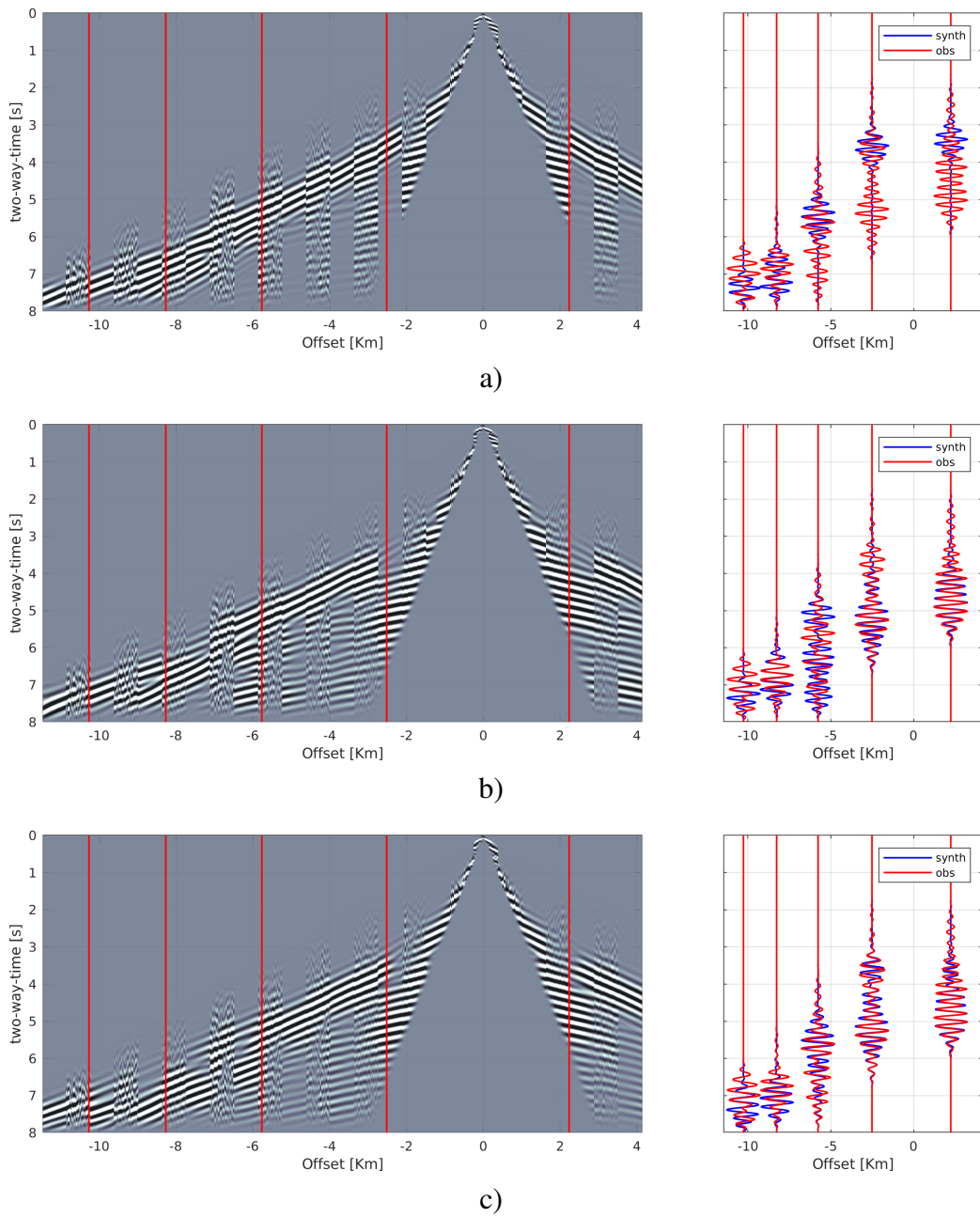


Figure 14: Data fit QC on common receiver gather away from the low-velocity cloud (cable B, Figure 1): a) Initial, b) Initial after short-offset diving wave FWI and  $I_p$  WI; c) GSOT JFWI. Synthetic and observed data alternate in the greyscale image with a 15-trace interval. Fit improves as continuities of seismic events increases. On the left, selected wiggle traces at the positions indicated by the red vertical lines in the greyscale plot

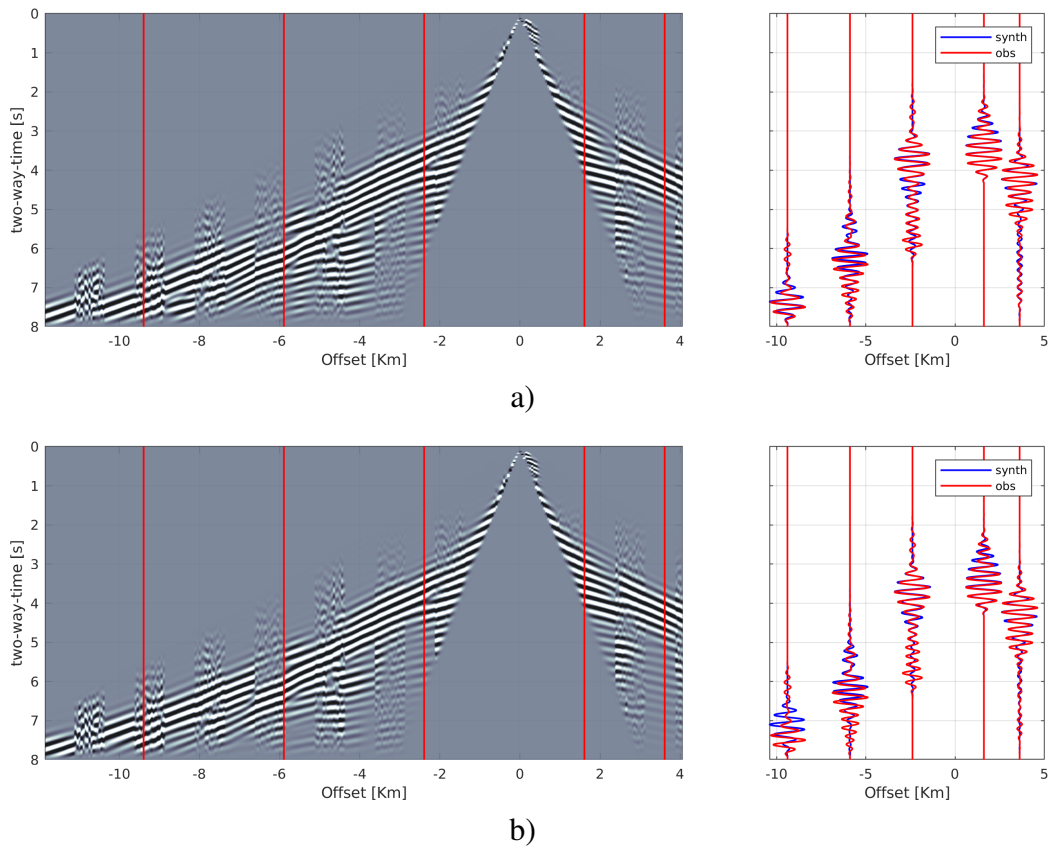


Figure 15: Data fit QC on common shot gather close to the low-velocity cloud (cable A). Comparison between FWI starting from the JFWI model (a) and layer-stripping conventional FWI starting from initial model (Pladys et al., 2022) (b).

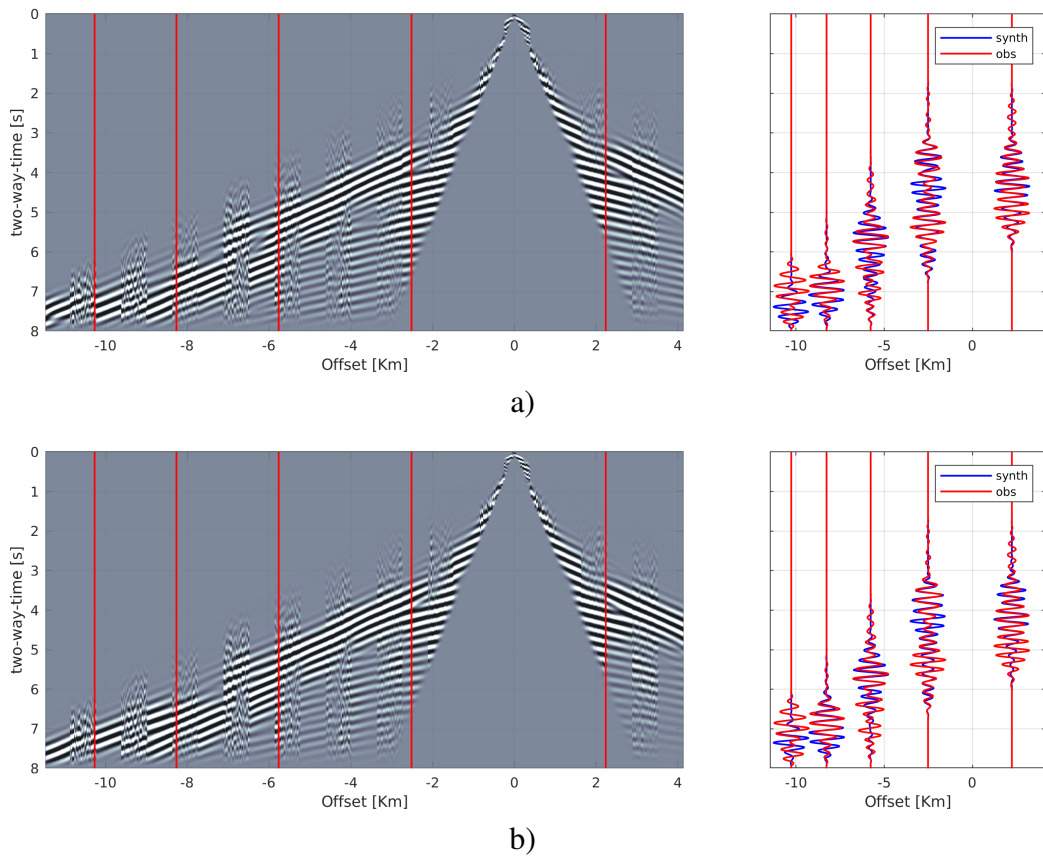


Figure 16: Data fit QC on common shot gather away from the low-velocity cloud (cable B). Comparison between FWI starting from the JFWI model (a) and layer-stripping conventional FWI starting from initial model (Pladys et al., 2022) (b).

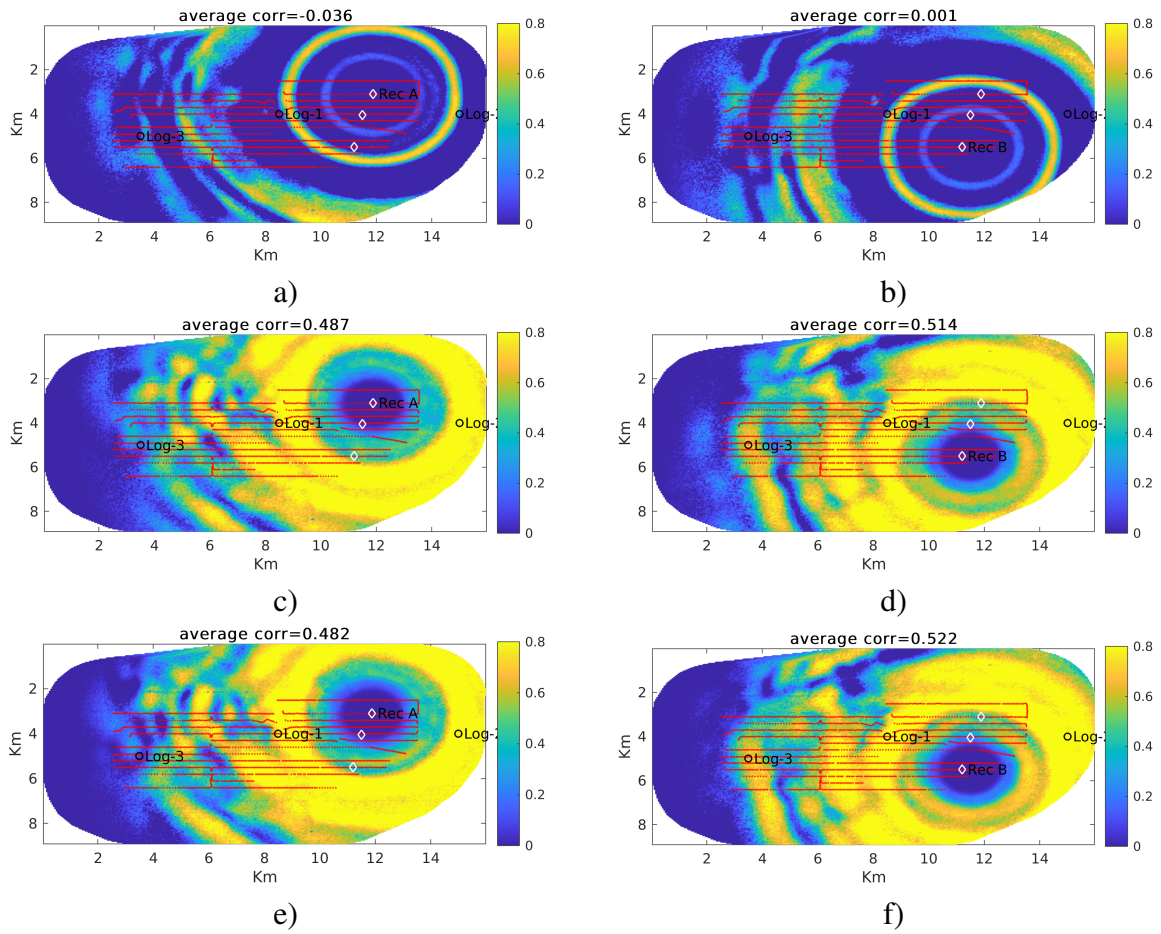


Figure 17: Cross-correlation of field and predicted data with a, b) initial model, c, d) FWI starting from initial model, e, f) FWI starting from JFWI model

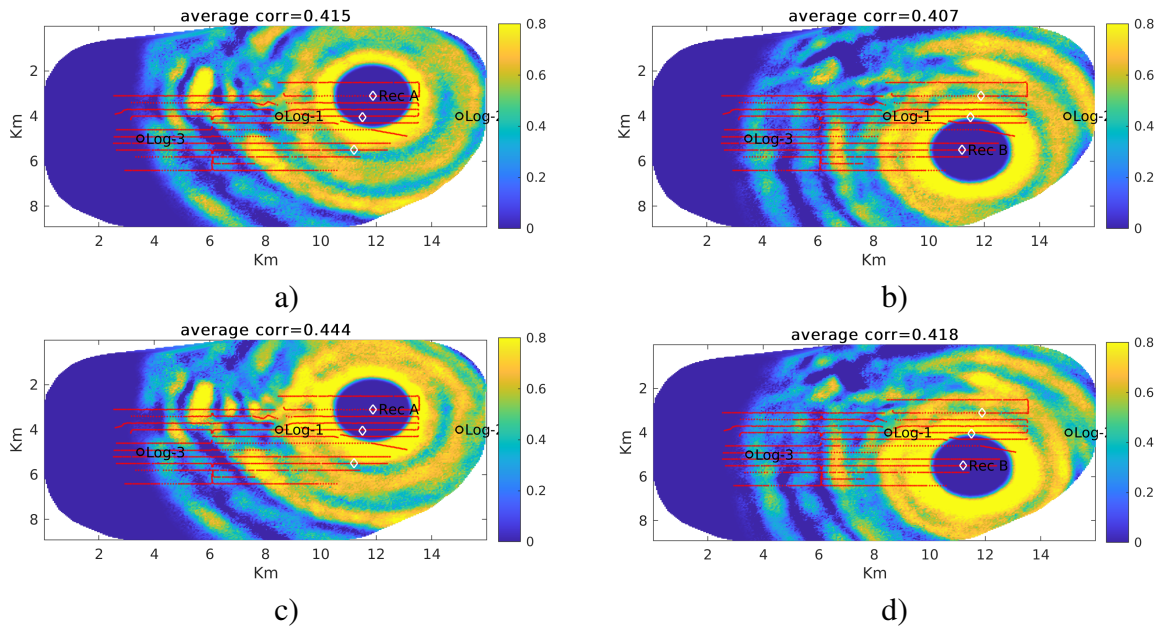


Figure 18: Cross-correlation of field and predicted data in the reflection window, with a, b) FWI starting from initial model, c, d) FWI starting from JFWI model

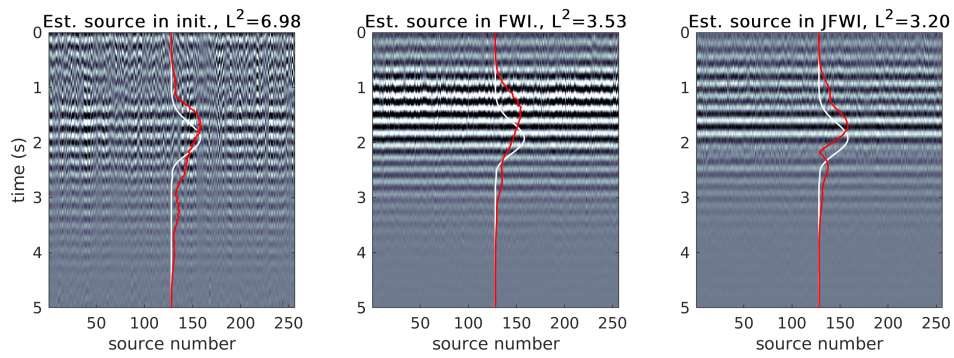


Figure 19: Source estimation quality check. The stationarity of the source wavelets estimated on different shots, at different locations should improve as the model quality increases, i.e. as the estimated model approximates the true one.  $L^2$  value refers to the variance of the estimate. Red line is the envelope of the average wavelet of each panel, white one is the envelope of the reference wavelet estimated on the short-offset early arrivals only for inversion.

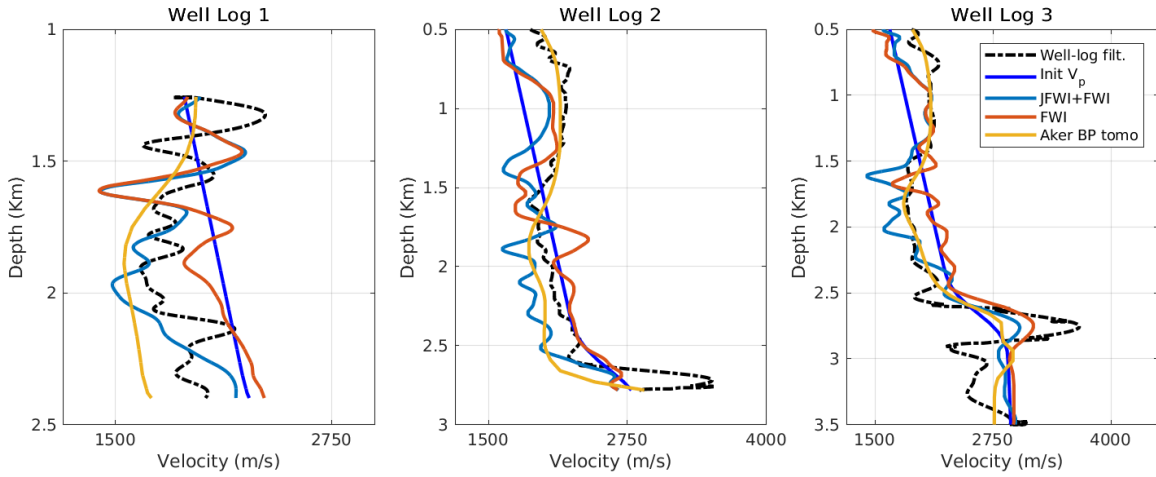


Figure 20: Well log predictions by JFWI+FWI and FWI using GSOT. Log P-wave velocities are converted to time, low-pass filtered within half a period for the maximum modelling frequency (5 Hz), and converted back to depth. Logs positions are plotted over the 1 km depth slice in Figure 1

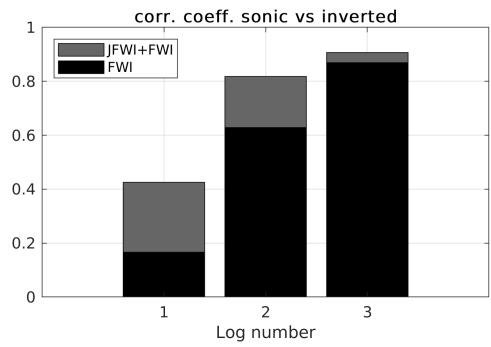


Figure 21: Correlation coefficient between low-pass filtered logs and inverted velocities at the same location. Note that, although in Log-2 FWI is closer to the ground-truth than JFWI (Figure 20), the correlation coefficient is larger for JFWI, probably resulting from a better prediction of the velocity changes with depth.

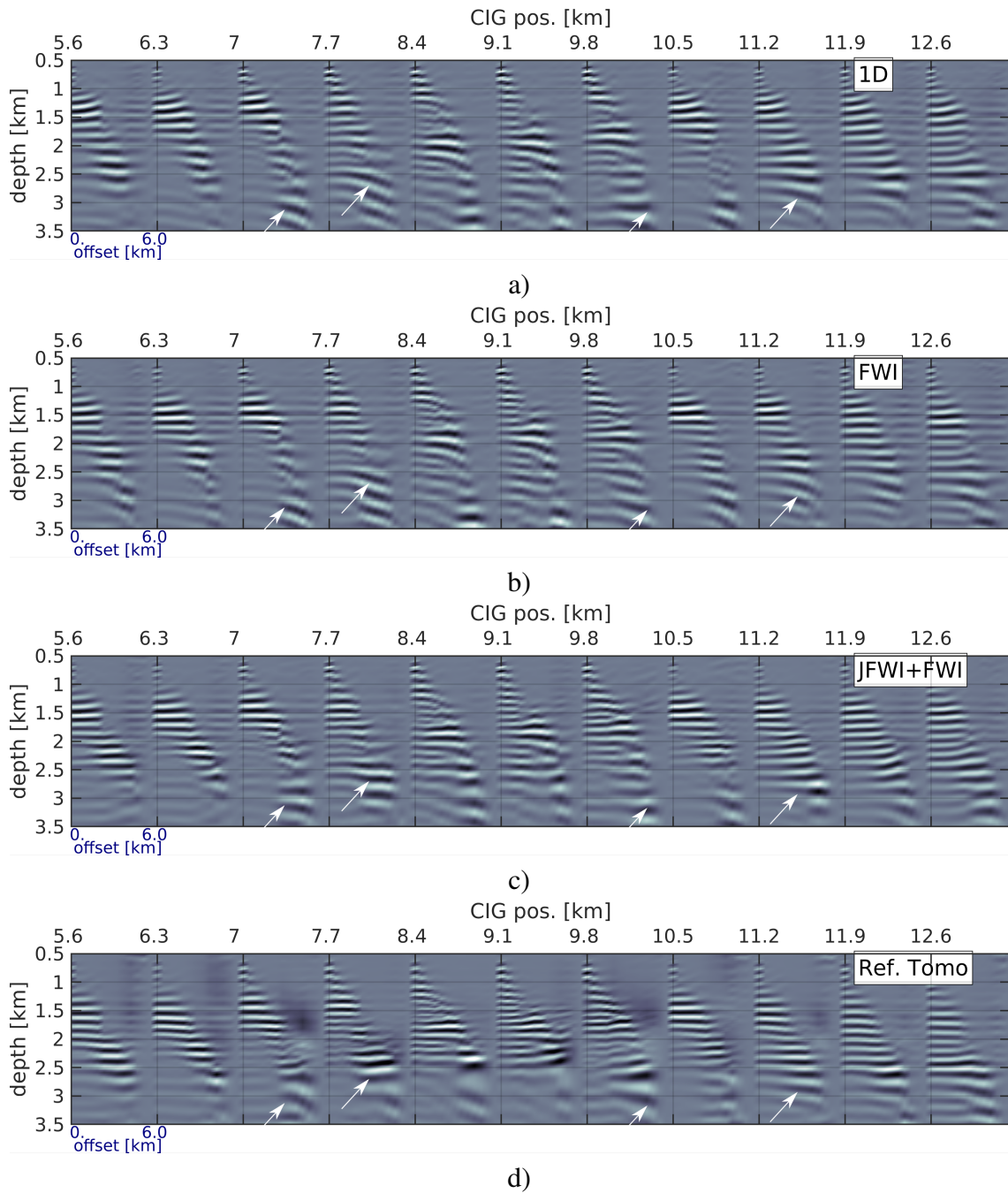


Figure 22: 2D RTM CIG gathers along cable A at offsets between 0 and 6 km. a) Initial 1D model; b) FWI starting from the 1D model; c) JFWI+FWI starting from the 1D model; d) Reference tomography model by Aker BP. The upper x-axis indicates the position of the CIG along cable A.

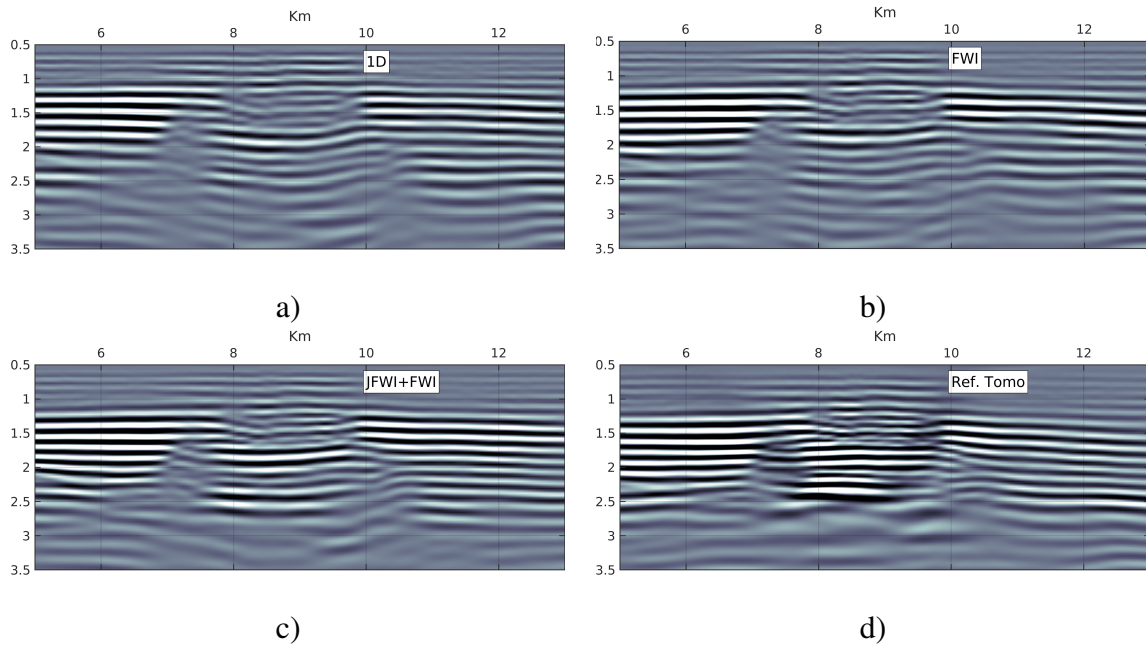


Figure 23: RTM 2D images along cable A. a) Initial 1D model; b) FWI starting from the 1D model; c) JFWI+FWI starting from the 1D model; d) Reference tomography model by Aker BP

## LIST OF TABLES

1	Inversion parameters for each step of the velocity-model building strategy, starting from the one-dimensional model. Gaussian smooth lengths are normalized by the local wavelength. $Z$ is the vertical dimension, positive downwards. While for JFWI $W_e, W_r$ are the relative weights of early arrivals and reflections in the joint objective function, in the FWI and $I_p$ WI steps they simply refer to the data misfit weighting (e.g. containing reflections only in $I_p$ WI). <u>Energy</u> preconditioning refers to scaling for the incident wavefield energy (Kamath et al., 2021), whereas <u>Asy</u> indicates the proposed asymptotic preconditioner for $I_p$ WI . . . . .	73
---	--	----

Stage	Max. offset	Smooth Z,X,Y/ $\lambda$	Precond.	Misfit	$W_e, W_r$	$\Delta^e T$	$\Delta^r T$
EWI	4.8 km	1.0, 1.0	Energy	GSOT	1, 0	0.35	–
$I_p$ WI	3 km	0.3, 0.8	Asy	$L^2$	0, 1	–	–
JFWI-1	7 km	0.4, 1.0	$z^1$	GSOT	1, 0.5	0.35	0.35
JFWI-2	9 km	0.4, 0.9	$z^{1.5}$	GSOT	1, 1	0.35	0.35
JFWI-3	All	0.3, 0.9	$z^2$	GSOT	1, 1	0.25	0.125
FWI-1	9 km	0.3, 0.8	Energy	GSOT	1, 1	0.25	–
FWI-2	All	0.3, 0.5	Energy	GSOT	1, 1	0.20	–

Table 1: Inversion parameters for each step of the velocity-model building strategy, starting from the one-dimensional model. Gaussian smooth lengths are normalized by the local wavelength. Z is the vertical dimension, positive downwards. While for JFWI  $W_e, W_r$  are the relative weights of early arrivals and reflections in the joint objective function, in the FWI and  $I_p$ WI steps they simply refer to the data misfit weighting (e.g. containing reflections only in  $I_p$ WI). Energy preconditioning refers to scaling for the incident wavefield energy (Kamath et al., 2021), whereas Asy indicates the proposed asymptotic preconditioner for  $I_p$ WI